

Dynamical Properties of the Molniya Satellite Constellation: Long-Term Evolution of the Semi-Major Axis

Jérôme Daquin (✉ daquin.jerome@gmail.com)

University of Namur <https://orcid.org/0000-0002-8931-7527>

Elisa Maria Alessi

IMATI CNR Milano: Istituto di Matematica Applicata e Tecnologie Informatiche Enrico Magenes
Consiglio Nazionale delle Ricerche Sezione di Milano

Joseph O'Leary

EOS

Anne Lemaitre

University of Namur: Universite de Namur

Alberto Buzzoni

Osservatorio di Astrofisica e Scienza dello Spazio di Bologna

Research Article

Keywords: Molniya orbit, tesseral resonance, lunisolar resonance, hyperbolic sets, space situational awareness

Posted Date: March 16th, 2021

DOI: <https://doi.org/10.21203/rs.3.rs-295816/v1>

License:  This work is licensed under a Creative Commons Attribution 4.0 International License.

[Read Full License](#)

Version of Record: A version of this preprint was published at Nonlinear Dynamics on July 26th, 2021.
See the published version at <https://doi.org/10.1007/s11071-021-06708-5>.

1 **Dynamical properties of the Molniya satellite constellation:**
2 **long-term evolution of the semi-major axis**

3 **Jérôme Daquin · Elisa Maria Alessi · Joseph**
4 **O’Leary · Anne Lemaitre · Alberto Buzzoni**

5
6 March 3, 2021

7 **Abstract** We describe the phase space structures related to the semi-major axis of Molniya-like
8 satellites subject to tesseral and lunisolar resonances. In particular, we dissect the indirect inter-
9 play of the critical inclination resonance on the semi-geosynchronous resonance using a hierarchy
10 of more realistic dynamical systems, thus discussing the dynamics beyond the integrable approx-
11 imation. By introducing *ad hoc* tractable models averaged over the fast angles, we numerically
12 demarcate the hyperbolic structures organising the long-term dynamics via the computation of
13 finite-time variational indicators. Based on the publicly available two-line elements space orbital
14 data, we identify two satellites, namely M1-69 and M1-87, displaying fingerprints consistent with
15 the dynamics associated to the hyperbolic set. The computations of the associated dynamical
16 maps highlight that the spacecraft are trapped within the hyperbolic tangle.

17 **Keywords** Molniya orbit · tesseral resonance · lunisolar resonance · hyperbolic sets · space
18 situational awareness

19 **1 Introduction**

This paper is part of a recent series of papers dedicated to properties and dynamics of Molniya spacecraft [1, 6, 29] with emphasis on the long-term evolution of the semi-major axis. We approach the problem by studying the long-term and drag-free motion of a test-particle subject to the non-spherical geometry of the Earth and third-body perturbations due to the Sun and the Moon. The metrical Keplerian prototypical values, semi-major axis a (expressed in units of Earth radius, r_E), eccentricity e and inclination i , considered in this work are

$$\alpha_{\mathcal{M}} = (a_{\mathcal{M}}, e_{\mathcal{M}}, i_{\mathcal{M}}) \sim (4.16 r_E, 0.7, 63.4^\circ). \quad (1)$$

Jérôme Daquin
Department of Mathematics (naXys), 61 Rue de Bruxelles, 5000, Namur, Belgium
E-mail: jerome.daquin@unamur.be

Elisa Maria Alessi
Istituto di Matematica Applicata e Tecnologie Informatiche “Enrico Magenes”, Consiglio Nazionale delle Ricerche,
Via Alfonso Corti 12, 20133 Milano, Italy
Istituto di Fisica Applicata “Nello Carrara”, Consiglio Nazionale delle Ricerche, Via Madonna del Piano 10, 50019
Sesto Fiorentino, Italy

Joseph O’Leary
EOS Space Systems Pty. Ltd., Lot Fourteen, McEwin Building, North Terrace, Adelaide, SA 5000, Australia
School of Information Technology and Mathematical Sciences, University of South Australia, GPO Box 2471,
Adelaide, SA, 5001, Australia

Anne Lemaitre
Department of Mathematics (naXys), 61 Rue de Bruxelles, 5000, Namur, Belgium

Alberto Buzzoni
INAF-OAS, Osservatorio di Astrofisica e Scienza del Spazio, Via P. Gobetti 93/3, 40129 Bologna, Italy

20 The zonal geopotential terms are restricted to the second degree J_2 term. Molniya satellites
 21 have a mean motion close to 2 revolutions per day and thus are subject to a 2 : 1 resonant
 22 commensurability with the Earth’s rotation rate (semi-synchronous orbits). Therefore, 12-hour
 23 resonant terms of the geopotential need to be taken into account to model the dynamics. The
 24 resonant terms are algebraically computed up to the 4th degree and order. Being interested in
 25 long-term dynamics, it is understood that we deal with the various Hamiltonian contributions
 26 averaged over the fast variables, leading to the so-called *secular* dynamics. The fast timescales
 27 are connected to the mean anomaly of the test-particle and the Moon and the Sun, denoted re-
 28 spectively M, M_M, M_S . The averaged contributions are introduced as the direct computation of
 29 the integral with respect to the fast variables. For the zonal contribution, this averaging is per-
 30 formed in closed form with respect of the eccentricity. The quadrupolar lunisolar perturbations,
 31 depending respectively on M and M_M or M and M_S are doubly averaged, also in closed form
 32 with respect of the eccentricity. For the resonant contribution of the geopotential, the averaging
 33 requires some extra care. First, the averaging is not performed in closed form over the eccentricity.
 34 Instead, we employ a truncated series expansion, which, considering the highly eccentric nature of
 35 the orbit, is given to 4th order in the eccentricity. Second, the averaging is not performed over the
 36 variable M directly, as it would not take into account accurately the resonant dynamics. Instead,
 37 this step calls for the introduction of new slow/fast variables taking into account the very reso-
 38 nant nature of the problem [2]. Once those variables are recognised and introduced explicitly, the
 39 averaged contribution is obtained in the usual way, *i.e.*, by averaging over the (new) fast variables.
 40

41 Molniya orbits gather two distinct resonant phenomena¹, with quite distinct timescales, giving
 42 rise to interesting qualitative dynamical behaviour. Firstly, as we mentioned, they are affected by
 43 a 2 : 1 geopotential resonance. Secondly, their inclination close to the critical inclination value of
 44 63.4° place them near a so-called “inclination dependent only” lunisolar resonance [21]. Whilst the
 45 first affects the semi-major axis of the orbit, the lunisolar effect manifests primarily on the eccen-
 46 tricity of the orbit, which exhibits large oscillations. These pulsations contribute to modulate the
 47 (no-longer constant) coefficients of the tesseral problem; henceforth a coupling and indirect inter-
 48 play between the two resonances might happen. The seminal contributions regarding the tesseral
 49 and lunisolar problems are gathered in [12, 13], and in the PhD work of T. Ely [14], later extended
 50 to full papers [15, 16]. F. Delhaise, J. Henrad and A. Morbidelli [12, 13] have focused their study on
 51 the eccentricity, inclination and argument of perigee, without paying attention to the behaviour
 52 of the semi-major axis. T. Ely connected the resonant problem with large-scale chaos affecting
 53 the semi-major axis, including the disturbing effects of the lunisolar perturbation, but for orbital
 54 parameters which differ from Molniya orbit [14]. The secular dynamics of Molniya semi-major axis
 55 remains partially unexplored.
 56

57 The first contribution of this paper is to discuss the dynamics of the semi-major axis beyond
 58 the integrable picture. For this task, we rely on classical tools from nonlinear dynamics to portray
 59 the dynamical structures organising the long-term dynamics (Poincar e section, sections of finite-
 60 time variational indicators). The chaotic nature of eccentric and inclined orbits subject to tesseral
 61 resonances, often explained through an overlap of nearby resonances [9], has been known for some
 62 time in the context of tesseral resonances [8, 10, 14]. Nevertheless, as we will highlight, the extent of
 63 chaos affecting the semi-major axis phase space for Molniya satellites is much more limited in the
 64 range of $i \sim 63^\circ$ compared to the previously studied range of inclinations. In fact, large connected
 65 chaotic seas are absent from the dynamics. Yet, hyperbolic orbits still exist and surround the
 66 unperturbed separatrix as we will show.

67 The second contribution of this paper is to reveal the precise effects of this coupling on the
 68 dynamics of the semi-major axis. This is achieved via the introduction of several dynamical sys-
 69 tems, aiming at isolating gradually the various effects and couplings. The driving principle is to
 70 introduce basic dynamical models, with the lowest number of degree-of-freedom (DoF) possible,

¹ The force model we employed is discussed with more details in the appendix A. The resonant argument ω
 which appears in the expansion of the lunisolar Hamiltonian also appears in higher geopotential zonal terms. In
 this sense, Molniya orbits gather more than 2 resonant phenomena, being affected by zonal, tesseral and third-body
 resonances. Nevertheless, the effects of higher zonal terms on the semi-major dynamics are negligible for our study
 and timescale of interests as we will demonstrate later.

71 which still encapsulate the physics and long-term qualitative features of the dynamics. Molniya
 72 orbits have also received attentions in [34, 35], but predominantly oriented towards the description
 73 of the long-term evolution of the eccentricity. The authors have built simplified secular dynamical
 74 models, in the same spirit as “isolating” the building blocks of the dynamics and reconstructed
 75 the qualitative features of the eccentricity, inclination and argument of perigee observables. A
 76 few model generated orbits have been compared to the publicly available two-line element (TLE)
 77 datasets². We underline that our contribution is paying particular attention to the orbit of Molniya
 78 M1-69 (NORAD³ satellite catalog number 17078), left untouched in a previous study, as being “in
 79 the vicinity of the separatrix” [35]. TLEs remain mainly the sole reservoir of orbital data. Their
 80 name comes from their format: time epochs and various orbital informations are summarised in a
 81 standardised two-lines format bulletin (see, *e.g.*, [7, 31]). The TLEs result from observational mea-
 82 sures, coupled with an orbit determination process and numerical propagations performed with
 83 simplified theories of motion. In this respect, they form rather pseudo-observations instead of
 84 “pure” observational data. Approximately every 8 hours, the unclassified TLEs are released pub-
 85 licly. Molniya spacecraft have been tracked since the mid-70’s, thus providing a sufficient long-time
 86 interval of TLEs to appreciate secular effects acting on the semi-major axis.

87 The third and final contribution of this paper is the clear connection of the dynamics of two
 88 satellites, Molniya M1-69 and Molniya M1-87 (with NORAD satellite catalog number 22949), with
 89 the fingerprints of the dynamics associated to the hyperbolic set. This last point sheds some light
 90 of the relevance of secular dynamical approaches and toolboxes for the field of space situational
 91 awareness and the continuing increasing space traffic. The patterns of the orbital semi-major axis
 92 time-series (extracted from the corpus of TLEs, more details will be presented in the subsequent)
 93 of the two aforementioned satellites are convincingly approached under this umbrella.

94 The paper is organised as follows:

- 95 1. In section 2, based on the Earth-only disturbing potential, a secular model is termed. A res-
 96 onant integrable system is formulated from which analytical quantitative estimates (width of
 97 the resonance, characteristic timescales) are extracted. This integrable picture is altered by a
 98 multiplet of resonances producing a separatrix splitting phenomena, responsible for the appari-
 99 tion of a chaotic layer in the phase space. For Molniya parameters, the overlap of resonances is
 100 complete. The corresponding 2-DoF Hamiltonian and its phase space is described via Poincaré
 101 sections.
- 102 2. In section 3, we introduce two models including lunisolar perturbations to overcome the limi-
 103 tations of the Earth-potential only based model. From these models, the effects of the lunisolar
 104 perturbations on the tesseral problem are studied. We use dynamical indicators to portray
 105 the phase space structures and reveal the hyperbolic set affecting the semi-major axis. The
 106 dynamics of the hyperbolic set is studied.
- 107 3. In section 4, after providing more information about the TLEs datasets, we connect the dynam-
 108 ics of the data for satellites M1-69 and M1-87 with the dynamics of the hyperbolic set. Relying
 109 on our understanding of the underlying dynamics, we extract specific epochs and orbital pa-
 110 rameters of the TLEs that spot the satellites within the hyperbolic tangle when computing
 111 their respective dynamical maps.

112 We close the paper by summarising our conclusions.

113 2 The secular and geopotential based Hamiltonian

114 We present our steps and assumptions to recover a relevant secular Hamiltonian model for 12-hour
 115 orbits based on the geopotential only and we describe the associated dynamics.

116 The disturbing potential of the Earth, in an Earth-centered and Earth-fixed frame, admits the
 following expansion [22]

$$V(r, \phi, \lambda) = V_Z(r, \phi) + V_T(r, \phi, \lambda), \quad (2)$$

² Available at space-track.org.

³ NORAD: North American Aerospace Defense Command.

with the zonal and tesseral parts respectively given by

$$\begin{cases} V_{\mathcal{Z}}(r, \phi) = \frac{\mu}{r} \sum_{l \geq 2} \left(\frac{r_{\text{E}}}{r}\right)^l J_{l,0} P_{l,0} \sin \phi, \\ V_{\mathcal{T}}(r, \phi, \lambda) = -\frac{\mu}{r} \sum_{l \geq 2} \sum_{m=1}^l \left(\frac{r_{\text{E}}}{r}\right)^l (c_{l,m} \cos m\lambda + s_{l,m} \sin m\lambda) P_{l,m}(\sin \phi), \end{cases} \quad (3)$$

117 where the vector (r, ϕ, λ) denote the spherical coordinates (respectively radius, latitude and longi-
118 tude), r_{E} denotes the mean Earth's radius, μ the gravitational parameter of the Earth. The $P_{l,m}$ are
119 the Legendre polynomials of degree l and order m . The coefficients $c_{l,m}$ and $s_{l,m}$ are the harmonic
120 coefficients describing Earth's gravity field where we denoted classically $J_{l,0} = -c_{l,0}$. Throughout
121 this paper, we denote the Keplerian orbital elements in the usual way as $(a, e, i, \omega, \Omega, M)$ where
122 a denotes the semi-major axis, e the eccentricity, i the inclination, ω the argument of perigee, Ω
123 the longitude of the ascending node and M the mean anomaly.

124 2.1 The secular zonal part

The zonal part is dominated by its quadrupole ($l = 2$) term and we therefore truncate $V_{\mathcal{Z}}$ to
 $l = 2$. Being interested by secular properties, the M -average of the J_2 part, defining the secular J_2
contribution, is computed (in closed form over the eccentricity) using the differential relationships

$$dM = \frac{r^2}{a\sqrt{1-e^2}} df, \quad (4)$$

together with the formula $r = a(1 - e^2)/(1 + e \cos f)$ (see *e.g.*, [22]):

$$\bar{V}_{J_2} = \frac{1}{2\pi} \int_0^{2\pi} V_{J_2} dM = \frac{1}{2\pi} \int_0^{2\pi} \frac{r^2}{a^2\sqrt{1-e^2}} V_{J_2} df. \quad (5)$$

The classical final expression (5), expressed in terms of the orbital elements, reads

$$\bar{V}_{J_2} = \frac{\mu r_{\text{E}}^2 J_2}{4a^3} (1 - e^2)^{-3/2} (3 \sin^2 i - 2). \quad (6)$$

125 Secular expressions of higher order terms and their effects are given in Appendix A for the sake of
126 completeness. From now on, we drop bars over averaged quantities, bearing in mind that we are
127 dealing with secular functions in this study.

128 2.2 The secular resonant tesseral part for 12-hour orbits

To compute the resonant secular contribution of the tesseral part

$$V_{\mathcal{T}} = \sum_{l \geq 2} \mathcal{T}_l, \quad (7)$$

with

$$\mathcal{T}_l = \sum_{m=1}^l -\frac{\mu}{r} \left(\frac{r_{\text{E}}}{r}\right)^l (c_{l,m} \cos m\lambda + s_{l,m} \sin m\lambda) P_{l,m}(\sin \phi), \quad (8)$$

129 we first express it in terms of the orbital elements using a series of formal substitutions. The
130 spherical coordinates are related to the orbital elements by:

$$\begin{cases} \cos(\alpha - \Omega) = \cos(\omega + f) / \cos \phi, \\ \sin(\alpha - \Omega) = \sin(\omega + f) \cos i / \cos \phi, \\ \sin \phi = \sin i \sin(\omega + f), \end{cases} \quad (9)$$

where α stands for the right ascension of the satellite (again, we refer to [22] for omitted details). The longitude λ is written as a function of α and the sidereal time θ as

$$\lambda = \alpha - \theta = (\alpha - \Omega) + (\Omega - \theta). \quad (10)$$

The sidereal time θ evolves linearly with time as $\theta = \varpi_E t$, with $\varpi_E = 2\pi/\text{sidereal day}$. Writing the inverse of the radius as

$$\frac{1}{r} = \frac{1 + e \cos f}{a(1 - e^2)}, \quad (11)$$

the quantities $\sin f$ and $\cos f$ are then written using their infinite series representation as a function of the mean anomaly M and the Bessel functions J_s (see, *e.g.*, [27])

$$\begin{cases} \sin f = \lim_{k \rightarrow +\infty} 2\sqrt{1 - e^2} \sum_{s=1}^k \frac{1}{s} \frac{d}{de} J_s(se) \sin sM, \\ \cos f = \lim_{k \rightarrow +\infty} -e + \frac{2(1 - e^2)}{e} \sum_{s=1}^k J_s(se) \cos sM. \end{cases} \quad (12)$$

Applying the aforementioned substitutions into Eq. (7) transforms it into an expression dependent solely on the orbital elements $(a, e, i, \Omega, \omega, M)$ and the sidereal time θ . The angles appear as linear combinations over the rationales of $M, \theta - \Omega$ and ω [22]. Computing at this stage the brute-force M -average to derive the secular tesseral contribution would suppress the dynamical effects of the resonant terms for 12-hour orbits. In fact, in the vicinity of 12-hour orbits, the fast angle

$$u_F = \theta - \Omega, \quad (13)$$

combines with the fast variable M as

$$2u_S = M - 2u_F, \quad (14)$$

to form a slow varying quantity. Therefore, in the neighborhood of 12-hour orbits, the variable u_S needs to be considered as a slow and independent variable. Dealing therefore with the variables u_F, u_S, ω , there is one fast angle u_F and two slow angles, ω and u_S . The resonant tesseral contribution is therefore obtained by averaging over the fast angle u_F as

$$\bar{V}_{\mathcal{T}} = \frac{1}{2\pi} \int_0^{2\pi} V_{\mathcal{T}} du_F. \quad (15)$$

The final expression has the form

$$\bar{V}_{\mathcal{T}} = \sum_{k=(k_1, k_2) \in K} h_k(a, e, i) \cos(\sigma_k + k_1 \lambda_{lm}), \quad K \subset \mathbb{Z}^2, \quad (16)$$

where

$$\sigma_k = k_1 u_S + k_2 \omega, \quad (17)$$

and λ_{lm} is a constant phase-term defined as

$$\begin{cases} c_{l,m} = -J_{lm} \cos m \lambda_{lm}, \\ s_{l,m} = -J_{lm} \sin m \lambda_{lm}. \end{cases} \quad (18)$$

131 In Tab. 1, we provide the final formal expression of the secular resonant terms⁴ for 12-hour
132 orbits up to $l = 4$ appearing in $\bar{V}_{\mathcal{T}}$ for the uplets $k \in K$ with Eq. (12) truncated to $k_{\max} = 4$.

133

⁴ Note that there are discrepancies with respect to the formulas presented in [8], imputable most probably to a systematic error in the implementation of the eccentricity functions.

$k = (k_1, k_2)$	$h_k(a, e, i)$	σ_k
(2, 0)	$-\frac{\mu r_{\text{E}}^2 J_{22} 9e(9e^2 - 8)(\cos i + 1)(\cos i - 1)}{32a^3}$	$M - 2\theta_S + 2\Omega$
(2, 2)	$\frac{\mu r_{\text{E}}^2 J_{22} 3e(e^2 - 8)(\cos i + 1)^2}{64a^3}$	$M - 2\theta_S + 2\Omega + 2\omega$
(2, -2)	$\frac{\mu r_{\text{E}}^2 J_{22} e^3(\cos i - 1)^2}{64a^3}$	$M - 2\theta_S + 2\Omega - 2\omega$
(2, -3)	$-\frac{\mu r_{\text{E}}^3 J_{32} 5e^4(\cos i - 1)^2 \sin i}{1024a^4}$	$M - 2\theta_S + 2\Omega - 3\omega$
(2, -1)	$\frac{\mu r_{\text{E}}^3 J_{32} 15e^2(49e^2 + 22)(3 \cos i + 1)(\cos i - 1) \sin i}{128a^4}$	$M - 2\theta_S + 2\Omega - \omega$
(2, 1)	$-\frac{\mu r_{\text{E}}^3 J_{32} 15(239e^4 + 128e^2 + 64)(3 \cos i - 1)(\cos i + 1) \sin i}{512a^4}$	$M - 2\theta_S + 2\Omega + \omega$
(2, 3)	$\frac{\mu r_{\text{E}}^3 J_{32} 5e^2(e^2 + 6)(\cos i + 1)^2 \sin i}{128a^4}$	$M - 2\theta_S + 2\Omega + 3\omega$
(2, 0)	$-\frac{\mu r_{\text{E}}^4 J_{42} 75e(27e^2 + 8)(21 \cos^2 i \sin^2 i - 7 \sin^2 i - 4 \cos^2 i + 4)}{256a^5}$	$M - 2\theta_S + 2\Omega$
(2, -2)	$\frac{\mu r_{\text{E}}^4 J_{42} 245e^3(\cos i - 1)(7 \cos i \sin^2 i - \cos i + 1)}{128a^5}$	$M - 2\theta_S + 2\Omega - 2\omega$
(2, 2)	$\frac{\mu r_{\text{E}}^4 J_{42} 15e(33e^2 + 8)(\cos i + 1)(7 \cos i \sin^2 i - \cos i + 1)}{128a^5}$	$M - 2\theta_S + 2\Omega + 2\omega$
(2, 4)	$\frac{\mu r_{\text{E}}^4 J_{42} 35e^3(\cos i + 1)^2 \sin^2 i}{512a^5}$	$M - 2\theta_S + 2\Omega + 4\omega$
(4, 0)	$\frac{\mu r_{\text{E}}^4 J_{44} 525e^2(31e^2 + 12)(\cos i - 1)^2(\cos i + 1)^2}{32a^5}$	$2(M - 2\theta_S + 2\Omega)$
(4, 2)	$-\frac{\mu r_{\text{E}}^4 J_{44} 105(65e^4 + 16e^2 + 16)(\cos i + 1)^3(\cos i - 1)}{64a^5}$	$2(M - 2\theta_S + 2\Omega) + 2\omega$
(4, 4)	$-\frac{\mu r_{\text{E}}^4 J_{44} 35e^2(2e^2 - 3)(\cos i + 1)^4}{32a^5}$	$2(M - 2\theta_S + 2\Omega) + 4\omega$

Table 1 Formal coefficients and resonant angles of the 2 : 1 resonance up to $l_{\text{max}} = m_{\text{max}} = 4$ and $\mathcal{O}(e^4)$.

Now that we have at hand the secular disturbing functions, the dynamics are cast into a Hamiltonian framework accounting for the Keplerian central part,

$$\mathcal{H} = \mathcal{H}_{\text{kep.}} + V_{J_2} + \mathcal{T}_2, \quad (19)$$

where \mathcal{T}_2 is obtained from (7) by restricting the expansion to $l = 2$. Note that \mathcal{T}_2 is $\mathcal{O}(e)$, whilst \mathcal{T}_3 and \mathcal{T}_4 are at least $\mathcal{O}(e^2)$ (except for the uplets (2, -1) and (4, 2)). The Hamiltonian must be a function of canonical variables who are presented hereafter. We mention however that we might sometimes refer to quantities expressed in orbital elements (non-canonical elements) and it is understood that the elements are themselves function of canonical variables.

2.3 Dynamics

We start by introducing the following canonical resonant coordinates

$$\begin{cases} I_1 = -L, & u_1 = 2\theta - \ell - 2h, \\ I_2 = G, & u_2 = g, \\ I_3 = H - 2L, & u_3 = h, \\ I_4 = -2L - \Gamma, & u_4 = -\theta, \end{cases} \quad (20)$$

where (L, G, H, ℓ, g, h) denote the classical canonical Delaunay variables related to the Keplerian elements by

$$\begin{cases} L = \sqrt{\mu a}, & \ell = M, \\ G = L \sqrt{1 - e^2}, & g = \omega, \\ H = G \cos i, & h = \Omega. \end{cases} \quad (21)$$

Given that the Hamiltonian (19) is time-dependent, $\dot{\theta} = \varpi_{\text{E}} = 2\pi/\text{sidereal day}$, we supplement the dynamics with 1-DoF given by the canonical conjugate variables denoted $(\Gamma, \tau = \theta)$, with

$\dot{\theta} = \dot{\tau} = \varpi_E$. Those variables enter into the definition of (I_4, u_4) . The autonomous dynamics (we still note \mathcal{H} the new Hamiltonian) reads

$$\mathcal{H} = \mathcal{H} + \varpi_E \Gamma. \quad (22)$$

140 The Hamiltonian (22) written in terms of the resonant coordinates (20) reduces to a 2-DoF system
 141 as both u_3 and u_4 are ignorable. Consequently, their conjugate canonical actions, I_3 and I_4 , are
 142 constant over time (*i.e.*, parameters). Note that when $u_2 = 0$, the problem is a 1-DoF problem
 143 and is therefore integrable.

144 2.3.1 The integrable approximation

When $u_2 \neq 0$, we derive the resonant integrable approximation assuming that the resonances are isolated [26]. It amounts to take into account in (19), besides the action-only dependent part, the harmonic with the largest amplitude (the *dominant term*, confer [8]). For Molniya's orbital parameters, $|h_{2,0}|$ is three times larger than $|h_{2,2}|$, and about 10^3 larger than $|h_{2,-2}|$. The 1-DoF approximation therefore reads

$$\tilde{\mathcal{H}} = \mathcal{H}_0 + h_{2,0} \cos(u_1 + 2\lambda_{22}). \quad (23)$$

The resonance $u_1 = 0$, that we denote \mathcal{R}_{u_1} , occurs for

$$\varpi_0(I_1) = \partial_{I_1} \mathcal{H}_0 = 0. \quad (24)$$

Solving this equation for fixed I_2, I_3 determined by $\alpha_{\mathcal{M}}$ expressed to the equivalent semi-major axis, we find

$$I_1 = I_1^* \leftrightarrow a_* = 26,555 \text{ km}. \quad (25)$$

For a 1-DoF system, orbits coincide with the set of level curves. The phase space is analogue to the classical pendulum dynamics. In fact, a Taylor expansion at order 2 of the Hamiltonian near $I_1 = I_1^*$ reduces the Hamiltonian to

$$\tilde{\mathcal{H}} = \frac{1}{2} \alpha_0 J_1^2 + h_{2,0} \cos(u_1 + 2\lambda_{22}), \quad (26)$$

where $J_1 = I_1 - I_1^*$ and

$$\alpha_0 = \partial_{I_1 I_1}^2 \mathcal{H}_0|_{I_1=I_1^*}. \quad (27)$$

Analytical characteristics of the resonance might be derived from (26). The equilibria are given by the solution of

$$\begin{cases} \dot{J}_1 = -\partial_{u_1} \tilde{\mathcal{H}} = h_{2,0} \sin(u_1 + 2\lambda_{22}) = 0, \\ \dot{u}_1 = \partial_{J_1} \tilde{\mathcal{H}} = \alpha_0 J_1 = 0, \end{cases} \quad (28)$$

leading to two the equilibrium solutions

$$\begin{cases} \mathbf{x}_s = (0, u_s = -2\lambda_{22}) \simeq (0, 3.66), \\ \mathbf{x}_u = (0, u_s = \pi - 2\lambda_{22}) \simeq (0, 0.52). \end{cases} \quad (29)$$

The eigensystem of the Jacobian matrix associated to (29) evaluated at the equilibrium solutions shows that \mathbf{x}_s is elliptic (stable fixed point) whilst \mathbf{x}_u is hyperbolic (unstable fixed point), from which emanates the separatrix. The eigensystem provides the characteristic periods of libration in the harmonic regime as

$$T_{\text{lib.}} = \frac{2\pi}{|\Im(\lambda_s)|} \simeq 1.76 \text{ years}. \quad (30)$$

The pair of eigenvalues $\pm\lambda_u$ associated with the unstable point \mathbf{x}_u defines an e-folding time T_e of

$$T_e = 1/|\lambda_u| \simeq 0.28 \text{ year}. \quad (31)$$

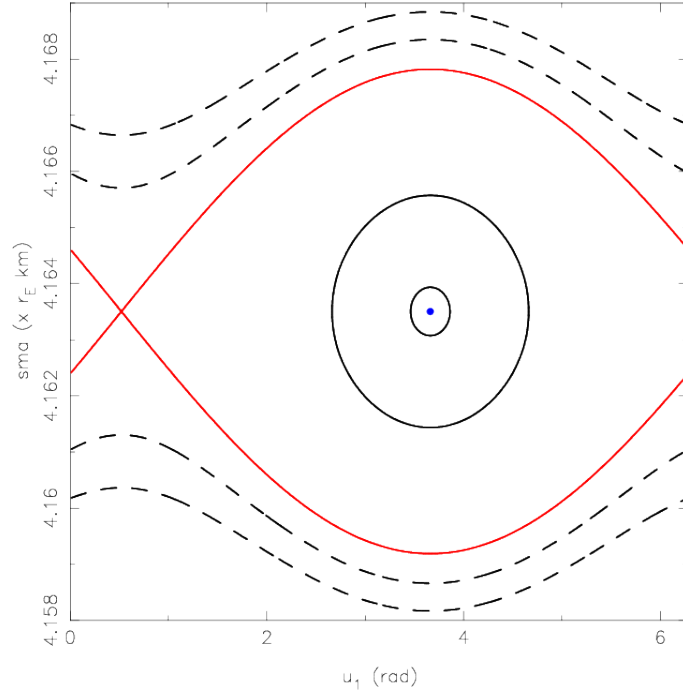


Fig. 1 Phase space of the resonant integrable approximation. The width of the separatrix (red curve) allows excursion of the semi-major axis up to $2\Delta a = 54$ km within the libration domain. The oscillations near the elliptic fixed-point (blue point) have a period of about 1.76 years.

The resonance half-width ΔJ_1 associated to (26), *i.e.*, the distance between $J_1 = 0$ and the apex of the separatrix (curve associated to the energy level of the unstable equilibria) satisfies

$$\tilde{\mathcal{H}}(\Delta J_1, u_s) = \tilde{\mathcal{H}}(0, u_u), \quad (32)$$

that is

$$\frac{1}{2}\alpha_0\Delta J_1^2 + h_{2,0} = -h_{2,0}. \quad (33)$$

Solving the last equality for ΔJ_1 , we find

$$\Delta J_1 = 2\sqrt{\frac{|h_{2,0}|}{|\alpha_0|}} \leftrightarrow \Delta a = 27 \text{ km}, \quad (34)$$

145 where the reader is referred to Fig. 1 for further qualitative details.

146 2.3.2 The 2-DoF picture

When $i_2 \neq 0$, the energy function (19) defines a 2-DoF problem with a multiplet of three resonances with critical angles $u_1, u_1 - u_2, u_1 + u_2$. Each isolated resonant problem admits its own pendulum reduction, with the possibility to overlap [9]. Analytical insights might be gained by some simplifications. In fact, let us approximate (19) with the following 2-DoF problem

$$\mathcal{K} = \frac{1}{2}\alpha_0 J_1^2 + \varpi_g \Gamma + h_{2,0} \cos(\phi) + h_{2,-2} \cos(\phi + 2\tau) + h_{2,2} \cos(\phi - 2\tau), \quad (35)$$

with $\phi = u_1 + 2\lambda_{22}$, where we have assumed the rate of variation of $u_2 = g$ to be ruled by the \mathcal{H}_{J_2} part, that is

$$i_2 \equiv \varpi_g = \frac{\partial \mathcal{H}_{J_2}}{\partial G} = \frac{3}{4} r_E^2 J_2 \frac{\mu^{1/2}}{a^{7/2}} \frac{5 \cos^2 i - 1}{(1 - e^2)^2} \Big|_{\alpha_{\mathcal{M}}}. \quad (36)$$

Therefore, u_2 is a pure time-like variable evolving linearly with time that we rename τ . Using the canonical equations, we find the three resonances centers of $\mathcal{R}_\phi, \mathcal{R}_{\phi+2\tau}, \mathcal{R}_{\phi-2\tau}$ to be located respectively at

$$\begin{cases} c_\phi(J_1) = 0, \\ c_{\phi+2\tau}(J_1) = -2\varpi_g/\alpha_0, \\ c_{\phi-2\tau}(J_1) = 2\varpi_g/\alpha_0. \end{cases} \quad (37)$$

The mutual distances of the center of the resonances with respect to the center of \mathcal{R}_ϕ ,

$$\begin{cases} \delta(\mathcal{R}_\phi, \mathcal{R}_{\phi+2\tau}) = |c_\phi - c_{\phi+2\tau}| = 2|\varpi_g/\alpha_0|, \\ \delta(\mathcal{R}_\phi, \mathcal{R}_{\phi-2\tau}) = |c_\phi - c_{\phi-2\tau}| = 2|\varpi_g/\alpha_0|, \end{cases} \quad (38)$$

are small given the proximity to the critical inclination. The corresponding δa amounts to be less than 1 km. Treated as isolated, the resonances $\mathcal{R}_\phi, \mathcal{R}_{\phi+2\tau}, \mathcal{R}_{\phi-2\tau}$ have the respective half-widths

$$\begin{cases} \Delta_{\mathcal{R}_\phi} = 2\sqrt{|h_{2,0}|/|\alpha_0|} \leftrightarrow \Delta_{\mathcal{R}_\phi} a = 27.5 \text{ km}, \\ \Delta_{\mathcal{R}_{\phi+2\tau}} = 2\sqrt{|h_{2,2}|/|\alpha_0|} \leftrightarrow \Delta_{\mathcal{R}_{\phi+2\tau}} a = 14.4 \text{ km}, \\ \Delta_{\mathcal{R}_{\phi-2\tau}} = 2\sqrt{|h_{2,-2}|/|\alpha_0|} \leftrightarrow \Delta_{\mathcal{R}_{\phi-2\tau}} a = 0.78 \text{ km}. \end{cases} \quad (39)$$

As inferred from the numerical computation of $h_{2,-2}$, the resonance $\mathcal{R}_{\phi-2\tau}$ is negligible for practical purposes. Due to the inequalities

$$\begin{cases} \Delta_{\mathcal{R}_\phi} + \Delta_{\mathcal{R}_{\phi+2\tau}} \gg \delta(\mathcal{R}_\phi, \mathcal{R}_{\phi+2\tau}), \\ \Delta_{\mathcal{R}_\phi} + \Delta_{\mathcal{R}_{\phi-2\tau}} \gg \delta(\mathcal{R}_\phi, \mathcal{R}_{\phi-2\tau}), \end{cases} \quad (40)$$

147 a complete resonance overlap takes place (*i.e.*, the resonances are strongly overlapped), by which
 148 is meant that the widths of the resonances (treated as isolated) are much larger than their mutual
 149 separations. This paradigm is encapsulated into an analogue of the so-called *modulated pendulum*
 150 *approximation* (see *e.g.*, [26]). From this analogy, we might infer the absence of large chaotic seas
 151 known to exist for similar eccentricity range but at lower inclination [10, 14]. Instead, we expect
 152 chaotic motions to appear only in the vicinity of the unperturbed separatrix [26, 28], with a librational
 153 region filled by stable orbits. This fact is indeed corroborated by computing the Poincaré
 154 map.

155

Stroboscopic map. The Hamiltonian (35) is a 1-DoF system periodically perturbed. Its phase space can be described by computing the associated Poincaré map, which is, given the periodic nature of the forcing, a stroboscopic mapping [25, 32]. Let us denote this mapping by \mathcal{P} and by $\mathcal{V}(0)$ a neighborhood of $J_1 = 0$. By defining the lift and projector operators respectively as

$$\begin{aligned} \mathfrak{l} : \mathcal{V}(0) \times [0, 2\pi] &\rightarrow \mathcal{V}(0) \times B \times [0, 2\pi]^2, \quad B \subset \mathbb{R}, \\ z = (J_1, u_1) &\mapsto \mathfrak{l}(z) = \mathbf{x} = (J_1, \Gamma, u_1, \tau), \end{aligned} \quad (41)$$

and

$$\begin{aligned} \mathfrak{p} : \mathcal{V}(0) \times B \times [0, 2\pi]^2 &\rightarrow \mathcal{V}(0) \times [0, 2\pi], \\ \mathbf{x} = (J_1, \Gamma, u_1, \tau) &\mapsto \mathfrak{p}(\mathbf{x}) = (J_1, u_1), \end{aligned} \quad (42)$$

the stroboscopic map is defined as

$$\begin{aligned} \mathcal{P} : \mathcal{V}(0) \times [0, 2\pi] &\rightarrow \mathcal{V}(0) \times [0, 2\pi], \\ z &\mapsto \mathcal{P}(z) = z' = \mathfrak{p} \circ \Phi^{T_g} \circ \mathfrak{l}(z), \end{aligned} \quad (43)$$

where Φ^t is the flow at time t associated to (35) and $T_g = 2\pi/\varpi_g$. Note that the lift is parameterised by the choice of $\tau(0) = g_0$. The “dummy” variable Γ does not enter into the equations of motion. For Molniya-like spacecraft, T_g defines a period of about 100 years (*i.e.*, the order of 10^4 orbital

revolutions). The mapping \mathcal{P} is constructed numerically based on the numerical propagation of the system (35). Given a value of g_0 , the coordinates of the fixed points of the mapping \mathcal{P} (*i.e.*, the periodic orbits of (35)) are determined using a Newton method. Due to the periodicity

$$\mathcal{K}(J_1, u_1; \tau) = \mathcal{K}(J_1, u_1; \tau + \pi), \quad (44)$$

the domain of g can be restricted to $[0, \pi]$. Let us recall that a fixed point z_* of \mathcal{P} , $\mathcal{P}(z_*) = z_*$, is hyperbolic when the linearisation has at least one eigenvalue with modulus greater than one. In case of complex eigenvalues, the fixed point is elliptic. For $g_0 = 0$, the two fixed points (semi-major axis given in km) read as

$$\begin{cases} \mathbf{x}_s = (a, u_1) = (26554.841, 3.662), \\ \mathbf{x}_u = (a, u_1) = (26554.850, 0.521). \end{cases} \quad (45)$$

Changing g_0 alters slightly those coordinates and the slope of the eigenvectors associated to the unstable periodic orbit, which may widen the aperture by a few kilometers. The stable and unstable manifolds associated to an hyperbolic point z_* ,

$$\begin{cases} \mathcal{W}^s(z_*) = \{z, \|\Phi^t(z) - z_*\| \rightarrow 0, t \rightarrow +\infty\}, \\ \mathcal{W}^u(z_*) = \{z, \|\Phi^{-t}(z) - z_*\| \rightarrow 0, t \rightarrow +\infty\}, \end{cases}$$

can be grown by iterating points belonging to the fundamental domain $I \subset E^{s,u}$, where $E^{s,u}$ are respectively the stable and unstable eigenspaces associated to z_* (and derived from the eigensystem analysis). Recall that $\mathcal{W}^{s,u}$ are locally tangent to $E^{s,u}$. In Fig. 2, we show the Poincar e section containing a chaotic zone surrounding the ‘‘unperturbed separatrix’’. A smaller portion of the phase space shows the first lobes associated to the stable manifold. The presence of a chaotic layer brings an important distinguishable qualitative feature to the dynamics: the semi-major axis might display intermittency phenomena (as for geosynchronous orbits, *confer* [5, 33]). More precisely, for initial conditions in the chaotic layer, the orbit swaps between the ‘‘inner-libration’’ (large range of variation of the semi-major axis), characterised by

$$\langle u_1 \rangle_{\text{lib.}} \simeq 0, \quad (46)$$

and the ‘‘outer-circulation’’ regime (smaller range of variation of the semi-major axis) for which

$$\langle u_1 \rangle_{\text{circ.}} \neq 0, \quad (47)$$

156 The alternation takes place when the orbit returns close enough to the hyperbolic saddle \mathbf{x}_u which
157 is discussed further in section 3.

The analysis of the eigensystem associated to the linearisation of \mathcal{P} at the saddle fixed-point is enlightening in deriving the Lyapunov timescale analytically. Let us recall that a Floquet characteristic exponent μ is a complex number satisfying

$$\lambda = e^{\mu T_g}, \quad (48)$$

where λ is an eigenvalue associated to the linearisation $D\mathcal{P}$ about the fixed point. For the hyperbolic saddle, the two eigenvalues $\{\lambda_1, \lambda_2 = 1/\lambda_1\}$ are real and so are the corresponding $\{\mu_1, \mu_2\}$, called in this case the Lyapunov exponents. From

$$\mu = T_g^{-1} \log \lambda, \quad (49)$$

158 the timescale of $1/\mu \sim 17$ years is derived for the largest eigenvalue. This timescale has been
159 compared with a brute-force estimation of the maximal Lyapunov exponents χ based on the vari-
160 ational dynamics (and their associated Lyapunov time $\tau_{\mathcal{L}} = 1/\chi$) in the vicinity of the hyperbolic
161 saddle. For hyperbolic orbits, we found Lyapunov times in the range of 15 – 18 years, this in very
162 good agreement with the analytical timescale based on $D\mathcal{P}$.

163

164 **Limitations of the model \mathcal{K} .** The model (35) is based on geopotential perturbations only. To
165 build a more realistic model, the lunisolar perturbations, Moon and Sun, need to be included. In
166 its present form, model \mathcal{K} is limited in two ways:

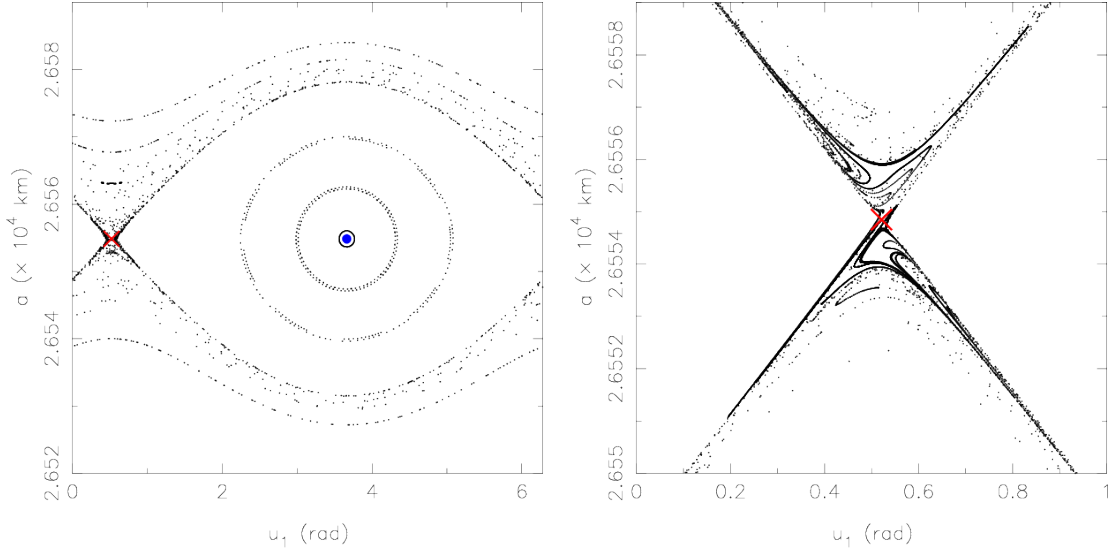


Fig. 2 (Left) Poincaré section associated to (35) computed for $g(0) = 0$. The unstable fixed point is labeled with the red cross, the blue circle surrounds the stable periodic orbit. The phase space is similar to the integrable approximation but contains a thin chaotic layer (scattered erratic points) surrounding the unperturbed separatrix. Each considered initial condition has been iterated 100 times under \mathcal{P} . (Right) Details of finite pieces of the stable manifold $\mathcal{W}^s(\mathbf{x}_u)$.

- 167 1. Under the lunisolar effects and due to the proximity to the critical inclination value, the
168 hypothesis that the argument of the perigee ($g = u_2$) flows linearly with time at a (constant)
169 rate given by the J_2 effect is violated.
- 170 2. The assumption that both the eccentricity and inclination are parameters is no longer true
171 under the influence of the lunisolar perturbation.

172 Increasing the complexity of the model gradually, we overcome the first limitation by decoupling
173 the equations of motions. We isolate a simplified energy function \mathcal{L} that dictates the time evolution
174 of the argument of perigee, $\dot{g} = \partial_G \mathcal{L}$, that we use to form a 6-dimensional dynamical system with
175 constant eccentricity and inclination. The variables (J_1, u_1) are then studied. The second limitation
176 is raised by introducing a 3-DoF Hamiltonian system, where both the eccentricity and inclination
177 vary according to the dynamics.

178 3 Secular Hamiltonian including lunisolar effects

179 3.1 The doubly-averaged lunisolar Hamiltonian

We adopt a simplified sub-model of the quadrupolar doubly-averaged formulation to model the external third-bodies perturbations. The quadrupolar approximation is commonly employed to study medium-Earth orbit dynamics and has already demonstrated its relevance (see *e.g.*, [17, 11]). Starting from the Hamiltonians

$$\begin{cases} \mathcal{H}_M = -\frac{\mu_M}{r_M} \left(\frac{r_M}{\|\mathbf{r} - \mathbf{r}_M\|} - \frac{\mathbf{r} \cdot \mathbf{r}_M}{r_M^2} \right), \\ \mathcal{H}_S = -\frac{\mu_S}{r_S} \left(\frac{r_S}{\|\mathbf{r} - \mathbf{r}_S\|} - \frac{\mathbf{r} \cdot \mathbf{r}_S}{r_S^2} \right), \end{cases}$$

where $\mathbf{r}_M, \mathbf{r}_S$ denote the geocentric vectors of the Moon and the Sun, r_M, r_S the corresponding geocentric distances and μ_M, μ_S their respective gravitational parameters, a Legendre-like expansion of \mathcal{H}_M and \mathcal{H}_S , truncated to $l = 2$ (*quadrupolar hypothesis*), and averaged over the mean anomalies (M, M_M) and (M, M_S) respectively, defines the so-called doubly averaged third-body model. This

averaging is performed in closed form over the eccentricity. Contrarily to the inner-perturbative part (geopotential), it requires to use the differential relationship

$$dM = (1 - e \cos E) dE, \quad (50)$$

coming from Kepler's equation (E refers to the eccentric anomaly). The double-averaging

$$\begin{cases} \mathcal{H}_M = \frac{1}{(2\pi)^2} \int_0^{2\pi} \int_0^{2\pi} \mathcal{H}_M dM dM_M = \frac{1}{(2\pi)^2} \int_0^{2\pi} \int_0^{2\pi} \mathcal{H}_M (1 - e \cos E) \frac{r_M^2}{a_M^2 \sqrt{1 - e_M^2}} dE df_M, \\ \mathcal{H}_S = \frac{1}{(2\pi)^2} \int_0^{2\pi} \int_0^{2\pi} \mathcal{H}_S dM dM_S = \frac{1}{(2\pi)^2} \int_0^{2\pi} \int_0^{2\pi} \mathcal{H}_S (1 - e \cos E) \frac{r_S^2}{a_S^2 \sqrt{1 - e_S^2}} dE df_S, \end{cases}$$

reduces \mathcal{H}_M and \mathcal{H}_S to an expansion of the form

$$\begin{cases} \mathcal{H}_M = h_0^M(a, e, i) + \sum_j h_j^M(a, e, i) \cos \phi_j^M, \\ \mathcal{H}_S = h_0^S(a, e, i) + \sum_j h_j^S(a, e, i) \cos \phi_j^S, \end{cases}$$

where ϕ_i^M and ϕ_j^S are permitted linear combinations of $(\omega, \Omega, \Omega_M)$ and (ω, Ω) respectively. Given that the angle Ω_M does not enter ϕ_j^S , the summations are homogenised by introducing ϕ_q , where

$$\phi_q = q_1 \omega + q_2 \Omega + q_3 \Omega_M, \quad (51)$$

with the convention that $q_3 = 0$ for the permissible solar arguments. The quadrupolar doubly-averaged lunisolar Hamiltonian reads therefore

$$\mathcal{H}_{MS} = \mathcal{H}_M + \mathcal{H}_S = (h_0^M + h_0^S) + \sum_{q \in \mathcal{Q}} (h_q^M + h_q^S) \cos \phi_q, \quad (52)$$

with (under the quadrupolar assumption)

$$\mathcal{Q} = \{q \in \mathbb{Z}_*^3 \mid q_1 \in \{-2, 0, 2\}, (q_2, q_3) \in \{-2, -1, 0, 1, 2\}^2\}. \quad (53)$$

For the sake of concision, let us denote $h_j^{MS} = h_j^M + h_j^S$. The Hamiltonian (52) is in general non-autonomous as time enters through the ecliptic precession of the lunar node, well-approximated by the linear law (Moon's elements are referred to the ecliptic plane)

$$\Omega_M \simeq \Omega_M(0) + \varpi_{\Omega_M} t, \quad (54)$$

180 where $2\pi/|\varpi_{\Omega_M}|$ defines a period of about 18.6 years. The Moon's inclination to the ecliptic plane
 181 is set to $i_M = 5^\circ 15'$. However, as we will see hereafter, the simplified model allowed by Molniya's
 182 parameters leads to a model independent of the argument of the Moon and, therefore, to an
 183 autonomous model.

184 3.2 Model for the time evolution of ω

The so-called ‘‘double resonance model’’ employed in [34] based on the lunisolar harmonics $\cos 2g$ and $\cos 2g \pm h$ have shown to provide a realistic model to capture the time evolution of the argument of perigee. They compared orbits generated using this model against TLEs data on several cases and were able to reproduce qualitatively the time evolution of the argument of perigee on several decades. More recently, [29] advocated that the $\cos h$ term produces a significant contribution to the dynamics of ω , where the reader is referred to Appendix A for further details. We adopt the following 2-DoF Hamiltonian system

$$\mathcal{L}(G, H, g, h) = \mathcal{L}_0(G, H) + \mathcal{L}_1(G, H, g, h), \quad (55)$$

$h_\sigma^M(a, e, i)$	σ	$h_\sigma^S(a, e, i)$	σ
$-\frac{15\mu_M a^2 e^2 \sin^2 i (3 \sin^2 \varepsilon - 2)(3 \sin^2 i_M - 2)}{64a_M^3 \eta_M^3}$	$2g$	$\frac{15\mu_S a^2 e^2 \sin^2 i (3 \sin^2 \varepsilon - 2)}{32a_S^3 \eta_S^3}$	$2g$
$-\frac{15\mu_M a^2 e^2 (\cos i + 1) \cos \varepsilon \sin i \sin \varepsilon (3 \sin^2 i_M - 2)}{32a_M^3 \eta_M^3}$	$2g + h$	$\frac{15\mu_S a^2 e^2 (\cos i + 1) \cos \varepsilon \sin i \sin \varepsilon}{16a_S^3 \eta_S^3}$	$2g + h$
$-\frac{15\mu_M a^2 e^2 (\cos i - 1) \cos \varepsilon \sin i \sin \varepsilon (3 \sin^2 i_M - 2)}{32a_M^3 \eta_M^3}$	$2g - h$	$\frac{15\mu_S a^2 e^2 (\cos i - 1) \cos \varepsilon \sin i \sin \varepsilon}{16a_S^3 \eta_S^3}$	$2g - h$
$\frac{3\mu_M a^2 (3e^2 + 2) \cos i \cos \varepsilon \sin i \sin \varepsilon (3 \sin^2 i_M - 2)}{16a_M^3 \eta_M^3}$	h	$-\frac{3\mu_S a^2 (3e^2 + 2) \cos i \cos \varepsilon \sin i \sin \varepsilon}{8a_S^3 \eta_S^3}$	h

Table 2 Formal expression of the lunar and solar coefficients associated to the harmonics $2g$, $2g \pm h$ and h . The obliquity of the ecliptic with respect to the equatorial plane is $\varepsilon = 23^\circ 44'$. The quantity i_M refers to the inclination of the Moon with respect to the ecliptic plane, $i_M = 5^\circ 15'$.

where

$$\begin{cases} \mathcal{L}_0 = \mathcal{H}_{J_2} + h_0^{\text{MS}}, \\ \mathcal{L}_1 = h_{2g}^{\text{MS}} \cos(2g) + h_{2g+h}^{\text{MS}} \cos(2g + h) + h_{2g-h}^{\text{MS}} \cos(2g - h), \end{cases}$$

to model the time evolution of ω . From the canonical equations derived from (55), we derive the dynamics of g . The formal coefficients appearing in (55), expressed using the Keplerian elements, are listed in table 2. The terms h_0^M and h_0^S refer to the action dependent only terms of \mathcal{H}_M and \mathcal{H}_S and read

$$\begin{cases} h_0^M = \frac{\mu_M a^2 (3e^2 + 2)(3 \sin^2 i - 2)(3 \sin^2 \varepsilon - 2)(3 \sin^2 i_M - 2)}{64a_M^3 \eta_M^3} \\ h_0^S = -\frac{\mu_S a^2 (3e^2 + 2)(3 \sin^2 i - 2)(3 \sin^2 \varepsilon - 2)}{32a_S^3 \eta_S^3}. \end{cases}$$

185 3.3 Effects of lunisolar perturbation on the tesseral dynamics

186 We investigate now how the lunisolar perturbation affects the hyperbolic structures of the tesseral
187 problem for Molniya parameters.

188 The basic model dictating the time evolution of g being established by (55), we focus now on
189 two dynamical systems improving the caveats of (35):

1. First, we introduce the differential system in \mathbb{R}^6 defined by the equations of motion (EoM):

$$\begin{cases} \dot{J}_1 = -\partial_{u_1} \mathcal{J}(J_1, u_1, g), \\ \dot{u}_1 = \partial_{J_1} \mathcal{J}(J_1, u_1, g), \\ \dot{G} = -\partial_g \mathcal{L}(G, H, g, h), \\ \dot{g} = \partial_G \mathcal{L}(G, H, g, h), \\ \dot{H} = -\partial_h \mathcal{L}(G, H, g, h), \\ \dot{h} = \partial_H \mathcal{L}(G, H, g, h). \end{cases} \quad (56)$$

where \mathcal{J} is defined as,

$$\mathcal{J}(J_1, u_1, g(t)) = \frac{1}{2} \alpha_0 J_1^2 + \mathcal{T}_2(u_1, g(t)). \quad (57)$$

190 Here \mathcal{L} is the basic lunisolar Hamiltonian function. For short, we refer to the EoM (56) as
191 model \mathcal{J} .

2. Second, we consider the 3-DoF Hamiltonian

$$\mathcal{S}(I_1, I_2, I_3, u_1, u_2, u_3) = \mathcal{H}_{\text{kep.}}(L) + \varpi_E \Gamma + \mathcal{T}_2(L, G, H, u_1, g) + \mathcal{L}(G, H, g, h), \quad (58)$$

expressed within the resonant coordinates. With respect to the model \mathcal{J} , model \mathcal{S} allows the action-terms to evolve under the correct dynamics. In particular, the tesseral coefficients $h_{2,0}(a, e, i)$, $h_{2,\pm 2}(a, e, i)$ appearing in the dynamics of (I_1, u_1) are no longer frozen (instead, they vary according to the changes of the Delaunay action vector (L, G, H)).

Let us emphasise that both models are π -periodic in g . Molniya spacecraft have, in general, $g \sim 270^\circ \pm 20^\circ$. For both models, in order to reveal the dynamical template and the possible intersection of hyperbolic structures with the (I_1, u_1) -plane, we compute the Fast Lyapunov Indicators (FLIs) associated to a 500×500 Cartesian mesh of initial conditions. The FLI is a variational tool that has been used on almost all astronomical scales, for applied or more theoretical oriented studies (see *e.g.*, [18, 24], and references therein). Let us recall that for an n -dimensional autonomous ordinary differential system defined on a open domain $D \subset \mathbb{R}^n$, $\dot{x} = f(x)$, the FLI at time t is derived from the linear map $D_x f$ at a point x :

$$\begin{aligned} D_x f : \mathbb{R}^n &\rightarrow \mathbb{R}^n, \\ w &\mapsto D_x f(x)w, \end{aligned} \quad (59)$$

and the associated variational equations

$$\begin{cases} \dot{x} = f(x), \\ \dot{w} = D_x f(x)w, \end{cases} \quad (60)$$

as

$$\text{FLI}(t) = \sup_{0 \leq \tau \leq t} \log(\|w(\tau)\|). \quad (61)$$

The vector $w \in \mathbb{R}^n$ denotes the tangent (or deviation) vector. The computation of the FLIs over resolved grid of initial conditions discriminates efficiently the structures of a given dynamical system, including the stable or unstable manifolds, ordered or chaotic seas. One advantage of the FLI over the characteristic Lyapunov exponent

$$\lambda(x, w) = \lim_{t \rightarrow +\infty} \frac{1}{t} \log(\|w(t)\|) \quad (62)$$

is to get rid of the time-average computation, thus speeding the stability determination process. The supremum appearing in (61) removes oscillations of the tangent vector. For regular orbits, the deviation vector grows linearly with time and therefore the FLI on regular KAM tori are characterised by values close to $\log(t_f)$. In hyperbolic regions, the norm of the tangent vector grows exponentially fast, and therefore the FLI display a linear trend surpassing quickly the value taken on KAM objects (see [3], chapter 5, for perturbative estimates).

The parametric dependence on t in (61) is raised after a calibration procedure. In our case, integration of several single orbits showed that $\tau_f = 20$ years are sufficient to obtain a sharp distinction. With our choice of units, the FLI on regular KAM tori is characterised by the value $\log(\tau_f) = 4.99$. The FLIs computation are performed for the vector fields $v_{\mathcal{J}}$ and $v_{\mathcal{S}}$ over a Cartesian discretisation of $\Sigma \subset \mathbb{R}^2$, where

$$\Sigma_{i_0} = \{(I_1, I_2, I_3, u_1, u_2, u_3) : (I_1, u_1) \in D, u_2 = 270^\circ, u_3 = 0, I_2 = 0.7, I_3(i_0) = H_\star - 2L_\star\}, \quad (63)$$

with

$$D = \mathcal{V}(I_1^\star) \times T, \quad T \subset [0, 2\pi]. \quad (64)$$

The neighborhood of the resonant action $\mathcal{V}(I_1^\star)$ represents typically a range of 70 km in the semi-major axis. Before commenting more on the results, let us mention a last point regarding the FLIs computation. We restricted the computations of the FLIs over Σ forward in time, *i.e.*, on a time interval $[0, \tau_f]$, $\tau_f > 0$, to obtain ‘‘positive in time FLIs’’, FLIs⁺. It is therefore understood that,

206 in the context of the existence of hyperbolic invariants, these computations on Σ would reveal the
 207 trace of the stable manifolds connected to the hyperbolic objects, *i.e.*, $\Sigma \cap \mathcal{W}^s$.

Similarly, backwards in time FLIs computed on Σ over $[-\tau_f, 0]$, FLIs^- , would reveal $\Sigma \cap \mathcal{W}^u$
 (or the hyperbolic chaotic sea in case of a strongly chaotic system). Both manifolds (henceforth,
 possible homoclinic or heteroclinic connections given the context), could be displayed on Σ by
 plotting the standard average

$$\text{FLI} = \frac{1}{2}(\text{FLI}^+ + \text{FLI}^-), \quad (65)$$

208 or any others weighted average (see *e.g.*, [18, 24]). We computed a few of those maps backwards
 209 in time, to display the averaged FLI. However, because we are not particularly interested of
 210 highlighting homoclinic connections and, more importantly, it does not change the dynamical
 211 mechanisms we are interested in, we present hereafter only the forward in time FLI maps (*i.e.*,
 212 we display FLI^+).

Our numerical campaign is parametric through 4 allowed values of i_0 , namely

$$i_0 \in \{62.5^\circ, 63.4^\circ, 64.3^\circ, 65.2^\circ\} \quad (66)$$

“piercing” the critical inclination value. This choice enters Σ_{i_0} through

$$I_3(i_0) = L_\star \sqrt{1 - I_2^2} \cos i_0 - 2L_\star, \quad I_2 = 0.7. \quad (67)$$

213 Although aware that the precise geometry of the hyperbolic structures depend on the initial
 214 phasing (ω, Ω) , our investigations focus on $(\omega, \Omega) = (270^\circ, 0)$. All the resulting maps of this
 215 numerical survey for models \mathcal{J} and \mathcal{S} are reported in Appendix C to ease the readability. We show
 216 hereafter in composite panels only the relevant information for the analysis. From this survey, we
 217 observe that:

- 218 1. Both models display a saddle-like point in Σ . This suggests the existence of an unstable periodic
 219 orbit (although this invariant has not been computed) for both flows, similar to the unstable
 220 periodic orbit we computed for model \mathcal{K} . Following this idea, the hyperbolic set (high values
 221 of FLIs with yellow color) emerging from the saddle-type structure is very likely to represent
 222 the intersections of the stable manifold of the hyperbolic invariant with Σ . The fine mesh of
 223 initial conditions allows to recognise lobes distinctively for model \mathcal{S} .
- 224 2. The model \mathcal{J} is overall weakly perturbed, and the hyperbolic layer is very close to the unper-
 225 turbed separatrix.
- 226 3. On the contrary, the hyperbolic layer of \mathcal{S} is much more developed. This fact is imputable
 227 to the indirect modulation of the coefficients $h_{2,0}(a, e, i)$ and $h_{2,\pm 2}(a, e, i)$ under the lunisolar
 228 effects. We therefore see the signature of the lunisolar coupling onto the tesseral problem.
- 229 4. In general, the width of the hyperbolic layer along a given line of u_1 increases with the values
 230 of i_0 . For u_1 within the stable librational domain (say $u_1 \sim 3.6$), the hyperbolic width along
 231 the line is about 1 km large in the semi-major axis ($i_0 = 62.5^\circ$) up to ~ 6 km large when
 232 $i_0 = 65.2^\circ$. For u_1 near the saddle, for the same inclination values, the hyperbolic layer foliates
 233 a width of about 10 km in the semi-major axis for $i_0 = 62.5^\circ$ and up to 30 km when $i_0 = 65.2^\circ$.
- 234 5. Lastly, and more will be commented on that in the following, we notice a growing asymmetry
 235 of the hyperbolic layer for increasing values of i_0 . At $i_0 = 65.2^\circ$, the hyperbolic layer is clearly
 236 more developed for the lower range of semi-major axis.

The dynamics associated with model \mathcal{S} is sketched and summarised within the composite panel
 in Fig. 3 based on the Hamiltonian model

$$\mathcal{T} = \frac{1}{2}A^2 + A_1 + \cos(\rho) + \epsilon \cos(\rho + \nu\rho_1), \quad (\epsilon, \nu) \in \mathbb{R}^2, \quad \nu \ll 1. \quad (68)$$

237 For $\epsilon = 0$, \mathcal{T} is integrable and has a saddle structure at $(A, \rho) = (0, \pi)$. The separatrix has a
 238 cat-eye topology with half-width $\Delta = 2\sqrt{2}$. When $\epsilon \neq 0, \epsilon \ll 1$, the resonances \mathcal{R}_ρ and $\mathcal{R}_{\rho+\nu\rho_1}$,
 239 ν -apart, produce a separatrix splitting. The resonant angle of an orbit with initial condition in
 240 the hyperbolic set alternates among libration, $\langle \rho \rangle \simeq 0$, and circulation, $\langle \rho \rangle \neq 0$. The “projection”
 241 of one orbit with initial condition close to the saddle (trapped in the hyperbolic tangle) in the

242 space (A, ρ) shows that the orbit remains mainly guided by the unperturbed separatrix. Under
 243 our selected initial condition, when the angle circulates, the action is trapped in the tangle, evol-
 244 ving here in the domain $\mathbb{A}^- := \{A, A < 0\}$. As soon as the $\langle \rho \rangle \neq 0$, the action experiences full
 245 homoclinic loops and evolve within $\mathbb{A} = \mathbb{A}^- \cup \mathbb{A}^+$. This process continues and possibly alternates
 246 in the vicinity of the unstable saddle, “kicking” the FLIs.

247

The dynamics associated to the hyperbolic layer of model \mathcal{S} is similar to the one just described, apart that the coefficients of the respective resonances are slowly modulated in time. This is exemplified for two orbits in the composite panel of Fig. 4, together with macro and micro views of the phase space structures. The orbit immersed within the stable region displays gentle oscillations, whilst the orbit trapped into the hyperbolic layer displays the characteristic intermittency. Let us underline that the hyperbolic orbit, on the 20 year timescale, displays U-turns (*i.e.*, the alternation between libration and circulation regimes of the resonant angle u_1) always directed towards lower semi-major axis, with a timescale of about 1.5 year. The full homoclinic loop takes about 3 years. We integrated the same orbit on a time interval 10 times larger and we noticed the unevenly distribution between upper and lower U-turns, the latter being more frequent. This property is clearly inferred from the thorough inspection and detailed geometry of the hyperbolic foldings near the saddle-like structure. The close-up view of the FLI map (see the magnified region materialised by the green box, Fig. 4) reveals more foldings in the lower part of the chart. Increasing the parametric value of i_0 makes this property even sharper, as shown in the maps provided in Appendix C. The asymmetry of the foldings emerges from the fact that

$$\delta(i_0) = \frac{|h_{2,0}(a, e, i)|}{|h_{2,2}(a, e, i)|}, \quad (69)$$

248 becomes larger along a solution $\mathbf{x}(t) = (a(t), e(t), i(t))$ for initial conditions near \mathbf{x}_u .

249

The layer’s dependence upon ω_0 , for model \mathcal{S} , is shown for the fixed value of $u_1 = 3.6$ in the last map of the composite plot of Fig. 4 (bottom right). It reveals a much wider width (roughly speaking on the order of 10 km in the semi-major axis) for $\omega \in [\pi, 3\pi/2]$, with petals structures. For $\omega \in [3\pi/2, \pi]$, the hyperbolic structure is much simpler to apprehend. For Molniya’s typical variation of $\omega \sim 270^\circ \pm 20^\circ$, this corresponds to the rectangle materialized with white dashed lines.

254

255 4 Connections and links with the dynamics of M1-69 and M1-87

256 On inspecting the extracted semi-major axis using M1-69 and M1-87 TLE data, we notice that
 257 they display intermittency phenomena on their semi-major axis⁵ as repeated in Fig. 5 and Fig. 6.
 258 The figures also incorporate the time evolution of the resonant angle u_1 . The relevant part of
 259 the data, in the light of the oscillating models previously derived, cover in both cases at least
 260 2 decades. Both data contain a transitory period, possibly remnants of unknown manoeuvres.
 261 For M1-87, after the epoch corresponding to mean Julian day (MJD) of 5.7×10^4 , the satellite
 262 experienced a significant semi-major axis reduction. We will not pay attention to this part of the
 263 data. In the exploitable window, the resonant signature, consisting of alternation between libration
 264 and circulation, is well-marked and in accordance with the U-turns intermittent semi-major axis
 265 variations. In both cases, the intermittency U-turns take place for $a \sim 26,550$ km, compatible
 266 with the locations of the hyperbolic foldings we located with model \mathcal{S} close to the saddle. It is
 267 worth mentioning that M1-69 has been left untouched in [34], as judged to “locate in the vicinity
 268 of this separatrix”. Below, we give more credit to this claim, and we show that it is also the case
 269 for its cousin M1-87. At the light of the dynamical mechanisms presented in section 3 and the
 270 fingerprints just described, it is tempting to say that both satellites evolve within the hyperbolic
 271 layer. To give more weight to this claim, we performed the following steps:

⁵ We extracted the mean semi-major axis (in the sense of the underlying SGP4 theory) from the TLEs by following the “un-Kozai” mean-motion procedure (one step iterative method) presented in [19], section 6. See also [30], Eq. (7) or [20], appendix B, section A.

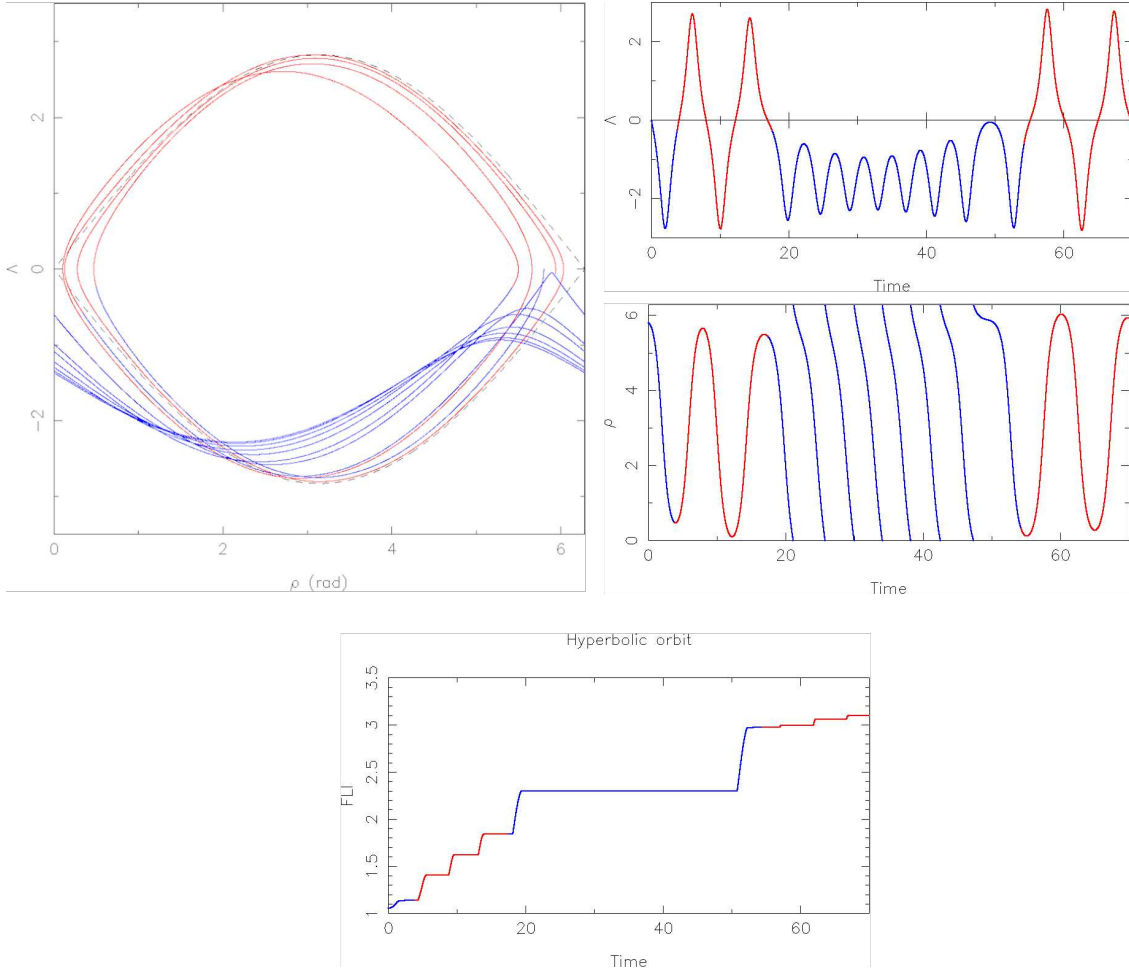


Fig. 3 Composite plot illustrating the mechanisms of the intermittency phenomena. The dashed black line represents the separatrix of the integrable model \mathcal{T} . Realisations of the stable and unstable manifolds, for $\epsilon \neq 0$, $\epsilon \ll 1$, are not shown for the sake of readability. One hyperbolic orbit trapped in the hyperbolic tangle is highlighted in the phase space, with a color code depending on the regime of the resonant angle. When the resonant angle circulates (blue color), $\langle \rho \rangle \neq 0$, the action takes negative Λ 's. When the angle librates (red color), $\langle \rho \rangle \simeq 0$, the action variable performs the full homoclinic loop and exhibit larger variations. Alternation between circulation and librations with passage close to the saddle contribute to breaks the plateau structure of the FLI and produces jumps in the FLI.

1. At epochs t_* corresponding to the apex of the first U-turns, we extract from the TLEs the corresponding orbital parameters and we record the values of (a^*, u_1^*) . For case M1-69, we selected $t_* = 50, 418.06$ (MJD), leading to the “instantaneous” elements

$$\begin{cases} a = 26,553.63 \text{ km}, & u_1 = 0.5257, \\ e = 0.67633, & \omega = 269^\circ 95, \\ i = 64^\circ 2544, & \Omega = 249^\circ 68. \end{cases} \quad (70)$$

For M1-87, we selected $t_* = 53, 433.24$ (MJD), for which the sets of computed elements reads

$$\begin{cases} a = 26,550.06 \text{ km}, & u_1 = 0.4749, \\ e = 0.6582, & \omega = 262^\circ 68, \\ i = 64^\circ 1995, & \Omega = 223^\circ 01. \end{cases} \quad (71)$$

- 272 2. We compute the dynamical structures with the FLIs for the vector field v_S , using as parameters
273 and phasing for Σ those extracted from the respective TLE at epoch t_* .

- 274 3. On the obtained dynamical maps, the point of coordinates $(a(t_*), u_1(t_*))$ is spotted.

275 The obtained dynamics maps shown in Fig. 7 convincingly demonstrate that the satellites reside
276 within the hyperbolic tangle.

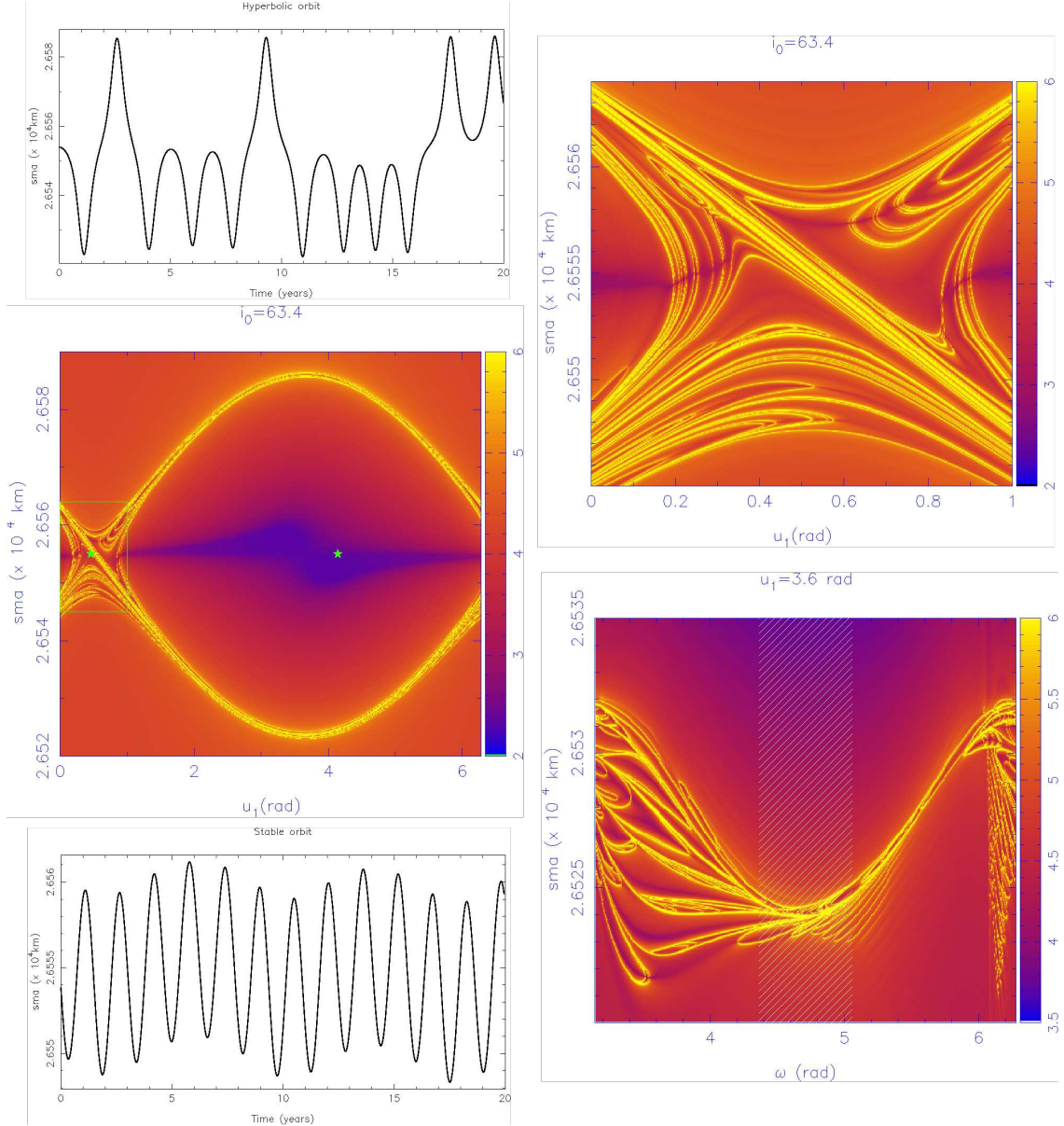


Fig. 4 Composite plot highlighting the main features of Molniya semi-major axis dynamics. The global FLI map and a magnified portion near the saddle-like structure detail the hyperbolic structure. Initial conditions within the hyperbolic layer display intermittency phenomena, whilst stable orbits display regular oscillations. This is exemplified for two orbits whose initial conditions are labeled with the green stars. The width of the layer, for a fixed u_1 but varying ω , might exhibit a complex geometry. For Molniya’s prototypical range of values of ω , materialised by the white shaded-line region around $\omega = 270^\circ$, the width is limited to a few kilometer in the semi-major axis only. See text for details.

277 5 Conclusions

278 The constructed dynamical models and their analysis allowed us to deepen the understanding of
 279 Molniya’s semi-major axis dynamics. The hyperbolic structures organising the phase space have
 280 been portrayed via variational indicators through a series of compact, tractable and realistic sec-
 281 ular models. The effect of lunisolar perturbations, on the 20 years timescale, needs to be taken
 282 into account to reconstruct the correct dynamical template. In fact, the induced modulations of
 283 the eccentricity and inclination contribute sufficiently to change the “parameters” of the tesseral
 284 problem; the coefficients we denoted by $h_{2,0}$ and $h_{2,\pm 2}$. We connected the 20 year long fingerprints
 285 of two satellites, Molniya 1-69 and Molniya 1-87, with the hyperbolic layer surrounding the unper-

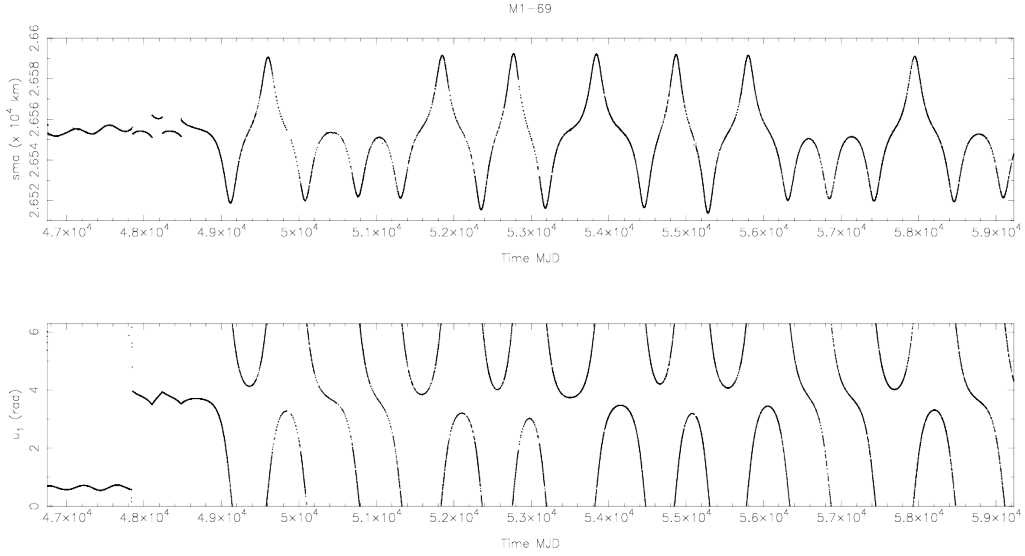


Fig. 5 Time history of the semi-major axis and resonant angle u_1 extracted from the TLE data for the satellite M1-69.

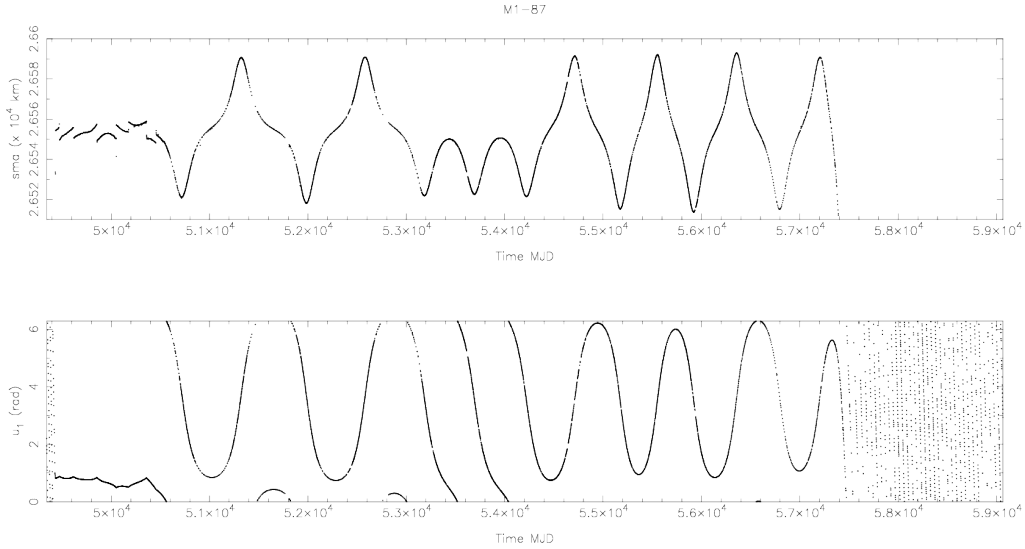


Fig. 6 Time history of the semi-major axis and resonant angle u_1 extracted from the TLE data for the satellite M1-87

286 turbed cat-eye separatrix. This hyperbolic layer, in absence of lunisolar perturbations, would be
 287 too thin to sustain the dynamical signatures visible at the publicly available data level. By com-
 288 puting their associated dynamical maps, we provided evidence that the two satellites are trapped
 289 within the hyperbolic tangle. The secular dynamics umbrella provided a reliable and robust mold
 290 to approach and explain the semi-major axis patterns extracted from the TLE space datasets. As
 291 far as we are aware, this result is the first report of long time scale hyperbolicity corroborated by
 292 pseudo-observations in the near-Earth space environment.

293 Acknowledgments

294 J.D. is a postdoctoral researcher of the “Fonds de la Recherche Scientifique” - FNRS. J.D. ac-
 295 knowledges discussions with Florent Deleflie, Denis Hautesseres, Alexis Petit and David Vallado
 296 about the TLEs data, and discussions that have followed from the CNES COMET-ORB work-
 297 shop on “Uncertainty Quantification in Orbit Propagation”, Feb. 9 – 10, 2021. J.D. acknowledges

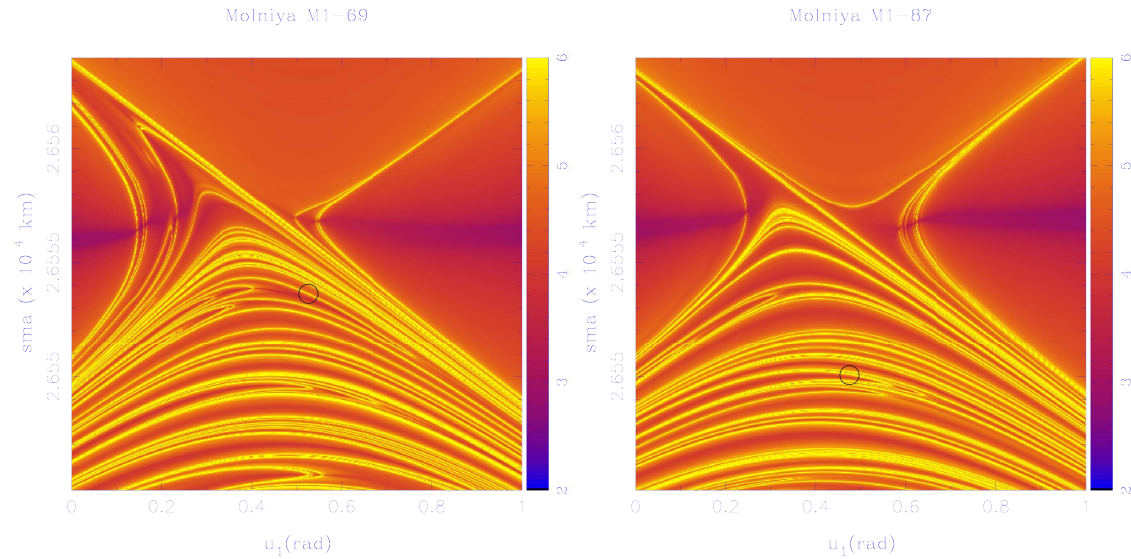


Fig. 7 Dynamical maps for Molniya M1-69 and M1-87. The locations of M1-69 and M1-87 are marked through the black circle. Both satellites reside within the hyperbolic tangle.

discussions with Ioannis Gkolias on the J_2^2 effect and useful references provided. J.D. acknowledges several discussions all along this research with Aaron Rosengren.

Conflict of interest

The authors declare that they have no conflict of interest.

References

1. Alessi, E.M., Buzzoni, A., Daquin, J., Carbognani, A., Tommei, G.: Dynamical properties of the molniya satellite constellation: Long-term evolution of orbital eccentricity. *Acta Astronautica* **179**, 659–669 (2021)
2. Beletsky, V.V.: *Essays on the motion of celestial bodies*. Birkh user (2012)
3. Benest, D., Lega, E., Froeschl , C.: *Hamiltonian systems and fourier analysis: new prospects for gravitational dynamics*. Cambridge Univ. Press (2005)
4. Breiter, S., M tris, G.: Symplectic mapping for satellites and space debris including nongravitational forces. *Celestial Mechanics and Dynamical Astronomy* **71**(2), 79–94 (1998)
5. Breiter, S., Wytrzyszczak, I., Melendo, B.: Long-term predictability of orbits around the geosynchronous altitude. *Advances in Space Research* **35**(7), 1313–1317 (2005)
6. Buzzoni, A., Guichard, J., Alessi, E.M., Altavilla, G., Figer, A., Carbognani, A., Tommei, G.: Spectrophotometric and dynamical properties of the soviet/russian constellation of molniya satellites. *Journal of Space Safety Engineering* **7**(3), 255–261 (2020)
7. Capderou, M.: *Handbook of satellite orbits: From kepler to GPS*. Springer Science & Business (2014)
8. Celletti, A., Gale , C.: On the dynamics of space debris: 1: 1 and 2: 1 resonances. *Journal of Nonlinear Science* **24**(6), 1231–1262 (2014)
9. Chirikov, B.V.: A universal instability of many-dimensional oscillator systems. *Physics reports* **52**(5), 263–379 (1979)
10. Daquin, J., Deleflie, F., P rez, J.: Comparison of mean and osculating stability in the vicinity of the (2: 1) tesseral resonant surface. *Acta Astronautica* **111**, 170–177 (2015)
11. Daquin, J., Gkolias, I., Rosengren, A.J.: Drift and its mediation in terrestrial orbits. *Frontiers in Applied Mathematics and Statistics* **4**, 35 (2018)
12. Delhaise, F., Henrard, J.: The problem of critical inclination combined with a resonance in mean motion in artificial satellite theory. *Celestial Mechanics and Dynamical Astronomy* **55**(3), 261–280 (1993)
13. Delhaise, F., Morbidelli, A.: Luni-solar effects of geosynchronous orbits at the critical inclination. *Celestial Mechanics and Dynamical Astronomy* **57**(1), 155–173 (1993)
14. Ely, T.A.: *Dynamics and control of artificial satellite orbits with multiple tesseral resonances*. Ph.D. thesis, Purdue University (1996)
15. Ely, T.A., Howell, K.C.: Dynamics of artificial satellite orbits with tesseral resonances including the effects of luni-solar perturbations. *Dynamics and Stability of Systems* **12**(4), 243–269 (1997)
16. Ely, T.A., Howell, K.C.: East–west stationkeeping of satellite orbits with resonant tesseral harmonics. *Acta Astronautica* **46**(1), 1–15 (2000)

- 334 17. Gkolias, I., Daquin, J., Gachet, F., Rosengren, A.J.: From order to chaos in earth satellite orbits. *The Astro-*
335 *nomical Journal* **152**(5), 119 (2016)
- 336 18. Guzzo, M., Lega, E.: Evolution of the tangent vectors and localization of the stable and unstable manifolds of
337 hyperbolic orbits by fast lyapunov indicators. *SIAM Journal on Applied Mathematics* **74**(4), 1058–1086 (2014)
- 338 19. Hoots, F.R., Roehrich, R.L.: Models for propagation of norad element sets. Tech. rep., Aerospace Defence
339 Command Peterson AFB Co Office Of Astrodynamics (1980)
- 340 20. Hoots, F.R., Schumacher Jr, P.W., Glover, R.A.: History of analytical orbit modeling in the us space surveillance
341 system. *Journal of Guidance, Control, and Dynamics* **27**(2), 174–185 (2004)
- 342 21. Hughes, S.: Earth satellite orbits with resonant lunisolar perturbations i. resonances dependent only on inclina-
343 tion. *Proceedings of the Royal Society of London. A. Mathematical and Physical Sciences* **372**(1749), 243–264
344 (1980)
- 345 22. Kaula, W.M.: *Theory of satellite geodesy*, blaisdell publ. Co., Waltham, Mass (1966)
- 346 23. Lara, M., San-Juan, J.F., Lopez-Ochoa, L.M.: Proper averaging via parallax elimination. *Advances in the*
347 *Astronautical Sciences* **150**, 315–331 (2014)
- 348 24. Lega, E., Guzzo, M., Froeschlé, C.: Theory and applications of the fast lyapunov indicator (fi) method. In:
349 *Chaos Detection and Predictability*, pp. 35–54. Springer (2016)
- 350 25. Meiss, J.: Symplectic maps, variational principles, and transport. *Reviews of Modern Physics* **64**(3), 795 (1992)
- 351 26. Morbidelli, A.: *Modern celestial mechanics: aspects of solar system dynamics* (2002)
- 352 27. Murray, C.D., Dermott, S.F.: *Solar system dynamics*. Cambridge university press (1999)
- 353 28. Murray, N., Holman, M.: Diffusive chaos in the outer asteroid belt. *The Astronomical Journal* **114**, 1246–1259
354 (1997)
- 355 29. Talu, T., Alessi, E.M., Tommei, G.: Investigation on a doubly-averaged model for the molniya satellites orbits.
356 arXiv preprint arXiv:2010.15746 (2020)
- 357 30. Vallado, D., Crawford, P.: Sgp4 orbit determination. In: *AIAA/AAS Astrodynamics Specialist Conference and*
358 *Exhibit*, p. 6770 (2008)
- 359 31. Vallado, D.A.: *Fundamentals of astrodynamics and applications*, vol. 12. Springer Science & Business Media
360 (2001)
- 361 32. Wiggins, S.: *Introduction to applied nonlinear dynamical systems and chaos*, vol. 2. Springer Science & Business
362 Media (2003)
- 363 33. Wytrzyszczak, I., Breiter, S., Borczyk, W.: Regular and chaotic motion of high altitude satellites. *Advances in*
364 *Space Research* **40**(1), 134–142 (2007)
- 365 34. Zhu, T.L., Zhao, C.Y., Wang, H.B., Zhang, M.J.: Analysis on the long term orbital evolution of molniya
366 satellites. *Astrophysics and Space Science* **357**(2), 126 (2015)
- 367 35. Zhu, T.L., Zhao, C.Y., Zhang, M.J.: Long term evolution of molniya orbit under the effect of earth’s non-
368 spherical gravitational perturbation. *Advances in Space Research* **54**(2), 197–208 (2014)

369 A Dynamical model employed & physical parameters

As we mentioned in the introduction, the aim of this study is not to study with the greatest accuracy possible Molniya dynamics, with a comprehensive force model including uncertainty modeling and Monte Carlo like approaches. Quite on the contrary, we leverage the understanding of the dynamics of the semi-major axis from the essential “building blocks” with tractable contributions. In that respect, we would like to provide more context to the dynamical model we have employed. We have approached the problem as a drag-free model, with no solar radiation pressure, based on a compact geopotential model including relevant terms of the disturbing lunisolar potentials. Higher order zonal secular terms can be obtained in closed form over the eccentricity following the same formal procedure discussed in Section 2.1. In terms of the orbital elements, up to order $l = 5$, they read:

$$\begin{cases} V_{J_3} = \frac{3J_3\mu r_E^3 e \sin i (5 \sin^2 i - 4)}{8a^4(1-e^2)^{5/2}} \sin(\omega), \\ V_{J_4} = \left(\frac{15J_4\mu r_E^4 \sin^2 i (7 \sin^2 i - 6)}{64a^5(1-e^2)^{7/2}} \right) \cos(2\omega) - \frac{3J_4\mu r_E^4 (3e^2 + 2)(35 \sin^4 i - 40 \sin^2 i + 8)}{128a^5(1-e^2)^{7/2}}, \\ V_{J_5} = \left(\frac{15J_5\mu r_E^5 e (3e^2 + 4) \sin i (21 \sin^4 i - 28 \sin^2 i + 8)}{128a^6(1-e^2)^{9/2}} \right) \sin(\omega) - \left(\frac{35J_5\mu r_E^5 e^3 \sin^3 i (9 \sin^2 i - 8)}{256a^6(1-e^2)^{9/2}} \right) \sin(3\omega). \end{cases}$$

It is worthwhile to note that the resonant argument of perigee also appears in the above secular contributions; hence the idea that Molniya orbits, besides tesseral and lunisolar resonances, gather also “zonal resonances”. To include the second-order part term with factor J_2^2 in the secular Hamiltonian, with the form

$$V_{J_2^2} = J_2^2 (A(a, e, i) \cos 2\omega + B(a, e, i)), \quad (72)$$

we used the formula given in [4, 23]. The relevance of our model \mathcal{S} has been assessed by including those effects, and the lunisolar $h_h^{\text{MS}} \cos h$ to \mathcal{L} . This model forms an “extended” Hamiltonian model $\tilde{\mathcal{S}}$. We computed the dynamical map for the Hamiltonian vector field $v_{\tilde{\mathcal{S}}}$ with $e = 0.7$, $i_0 = 64^\circ 3$ and $(\omega, \Omega) = (270^\circ, 0)$ and we did not noticed significant macroscopic changes in the obtained dynamical template; henceforth the relevance of the Hamiltonian model \mathcal{S} . Let us mention that even if the macroscopic structures do not change drastically, hyperbolic orbits

$k = (k_1, k_2)$	$h_k(a, e, i)$	σ_k
(1, 0)	$\frac{\mu r_E^2 J_{21} 9e \cos i \sin i}{4a^3}$	$M - \theta_S + \Omega$
(1, 2)	$\frac{\mu r_E^2 J_{21} 3e(\cos i + 1) \sin i}{8a^3}$	$M - \theta_S + \Omega + 2\omega$
(2, 0)	$-\frac{\mu r_E^2 J_{22} 27e^2 (\cos i + 1)(\cos i - 1)}{8a^3}$	$2(M - \theta_S + \Omega)$
(2, 2)	$-\frac{\mu r_E^2 J_{22} (5e^2 - 2)(\cos i + 1)^2}{8a^3}$	$2(M - \theta_S + \Omega + \omega)$
(1, -1)	$\frac{\mu r_E^3 J_{31} 33e^2 (15 \cos i \sin^2 i - 5 \sin^2 i - 4 \cos i + 4)}{128a^4}$	$M - \theta_S + \Omega - \omega$
(1, 1)	$-\frac{\mu r_E^3 J_{31} 3(2e^2 + 1)(15 \cos i \sin^2 i - 5 \sin^2 i - 4 \cos i - 4)}{16a^4}$	$M - \theta_S + \Omega + \omega$
(1, 3)	$\frac{\mu r_E^3 J_{31} 15e^2 (\cos i + 1) \sin^2 i}{16a^4}$	$M - \theta_S + \Omega + \omega$
(2, 1)	$-\frac{\mu r_E^3 J_{32} 45e(\cos i + 1)(3 \cos i - 1)}{8a^4}$	$2(M - \theta_S + \Omega) + \omega$
(2, 3)	$-\frac{\mu r_E^3 J_{32} 15e(\cos i + 1)^2 \sin i}{8a^4}$	$2(M - \theta_S + \Omega) + 3\omega$
(3, 1)	$\frac{\mu r_E^3 J_{33} 2385e^2 (\cos i + 1)^2 (\cos i - 1)}{64a^4}$	$3(M - \theta_S + \Omega) + \omega$
(3, 3)	$\frac{\mu r_E^3 J_{33} 15(6e^2 - 1)(\cos i + 1)^3}{8a^4}$	$3(M - \theta_S + \Omega) + 3\omega$
(1, 0)	$\frac{\mu r_E^4 J_{41} 75e \cos i \sin i (7 \sin^2 i - 4)}{16a^5}$	$M - \theta_S + \Omega$
(1, 2)	$-\frac{\mu r_E^4 J_{41} 5e \sin i (14 \cos i \sin^2 i + 7 \sin^2 i - 6 \cos i - 6)}{16a^5}$	$M - \theta_S + \Omega + 2\omega$
(2, 0)	$-\frac{\mu r_E^4 J_{42} 75e^2 (21 \cos^2 i \sin^2 i - 7 \sin^2 i - 4 \cos^2 i + 4)}{8a^5}$	$2(M - \theta_S + \Omega)$
(2, 2)	$-\frac{\mu r_E^4 J_{42} 15(e^2 + 1)(\cos i + 1)(7 \cos i \sin^2 i - \cos i - 1)}{4a^5}$	$2(M - \theta_S + \Omega) + 2\omega$
(2, 4)	$-\frac{\mu r_E^4 J_{42} 105e^2 (\cos i + 1)^2 \sin^2 i}{32a^5}$	$2(M - \theta_S + \Omega) + 4\omega$
(3, 2)	$\frac{\mu r_E^4 J_{43} 945e(\cos i + 1)^2 (2 \cos i - 1) \sin i}{16a^5}$	$3(M - \theta_S + \Omega) + 2\omega$
(3, 4)	$\frac{\mu r_E^4 J_{43} 315e(\cos i + 1)^3 \sin i}{32a^5}$	$3(M - \theta_S + \Omega) + 4\omega$
(4, 2)	$-\frac{\mu r_E^4 J_{44} 5565e^2 (\cos i - 1)(\cos i + 1)^3}{16a^5}$	$4(M - \theta_S + \Omega) + 2\omega$
(4, 4)	$-\frac{\mu r_E^4 J_{44} 105(11e^2 - 1)(\cos i + 1)^4}{16a^5}$	$4(M - \theta_S + \Omega) + 4\omega$

Table 3 Formal coefficients and resonant angles of the 1 : 1 resonance for $l_{\max} = m_{\max} = 4$ and up to $\mathcal{O}(e^2)$.

generated under model \mathcal{S} and $\tilde{\mathcal{S}}$ will separate in time (sensitivity to the slight change of physics), and the hope to follow them beyond a few Lyapunov times is a useless effort. The Lyapunov time $\tau_{\mathcal{L}}$ computed as

$$\begin{cases} \chi = \lim_{s \rightarrow +\infty} \frac{1}{s} \log(\|w(s)\|), \\ \tau_{\mathcal{L}} = 1/\chi, \end{cases}$$

370 is about 2 decades.

371

372

373 The physical parameters of this study read as follow. The Moon's orbital parameters, referred to the ecliptic
374 plane, have been set to $a_M = 384,748$ km, $e_M = 0.0554$, $i_M = 5^\circ 15'$, $\mu_M = 4902.8$ km³/s². The Sun's orbital
375 parameters, referred to the Earth equator, have been set to $a_S = 1.496 \times 10^8$ km, $e_S = 0.0167$, $i_S = 23^\circ 43' 29.11''$,
 $\mu_S = 1.32712 \times 10^{11}$ km³/s². The length unit is the Earth radius r_E of 6378.1363 km, $\mu = 398,600.44$ km³/s².

376 B Resonant potential for the geosynchronous tesseral resonance

377

378 As mentioned, expressions presented in [8] related to the tesseral resonant contributions contain slight algebraic
379 errors. We therefore present the algebraic expressions of the resonant tesseral associated to the geosynchronous
380 region (1:1 resonance) up to order $l = 4$. Orbits in this regime have smaller eccentricities and, as in [8], we truncate
381 the development in eccentricity to $k_{max} = 2$. To derive the resonant contribution for the geosynchronous region, we
382 follow identically the steps presented in subsection 2.2 apart that u_S reads now $u_S = M - u_F$, where $u_F = \theta - \Omega$.
383 Following our previous presentation, the formal coefficients and critical angles of $\mathcal{T}_2^{1:1}$, $\mathcal{T}_3^{1:1}$, $\mathcal{T}_4^{1:1}$ are compactly
384 summarised in Table 3 in terms of the Keplerian orbital elements. Let us recall that we denote by σ_k the critical
angle $\sigma_k = k_1 u_S + k_2 \omega = k_1(M - \theta_S + \Omega) + k_2 \omega$.

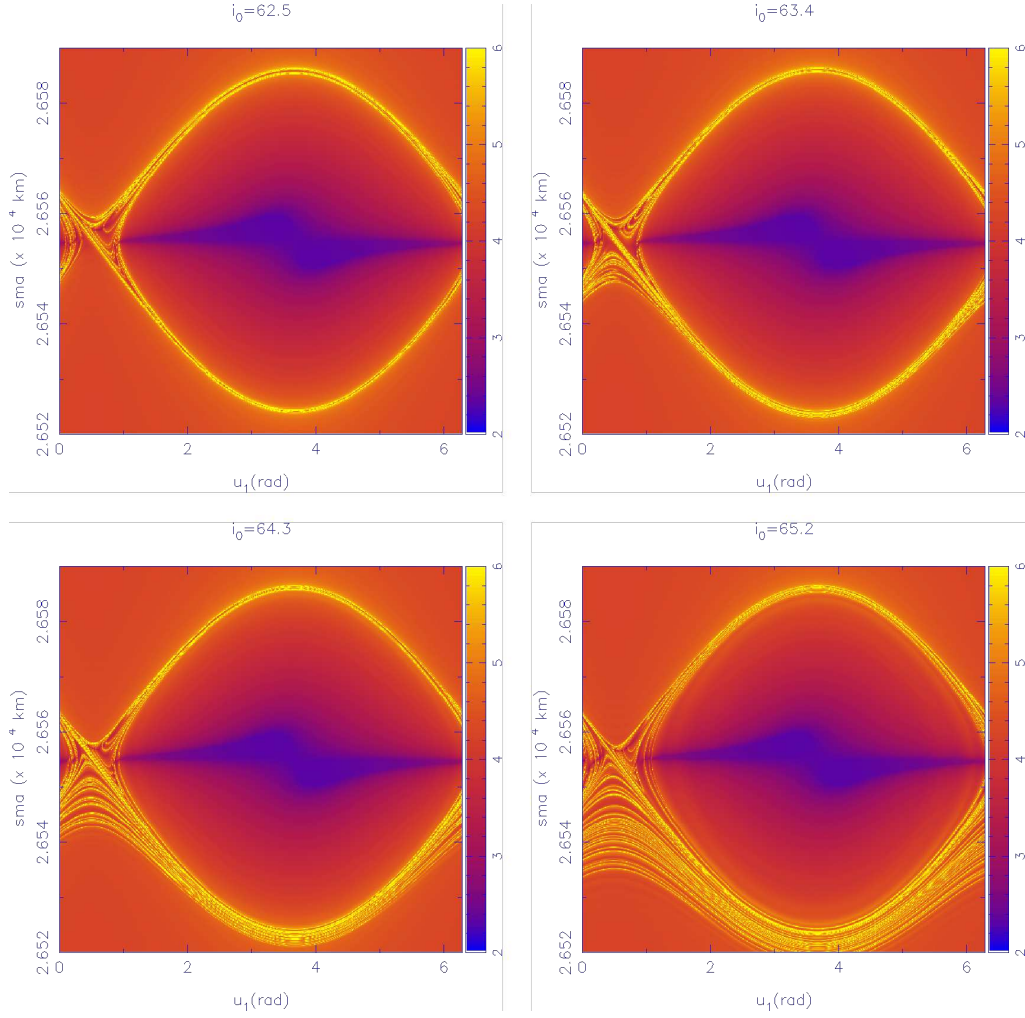


Fig. 8 Intersections of the forward in time FLIs with the plane (a, u_1) for model \mathcal{S} computed on a 500×500 grid of initial conditions for $i_0 \in \{62.5, 63.4, 64.3, 65.2\}$ deg.

385 C Dynamical maps

386 We computed dynamical maps for a fixed value of $e = 0.7$ and i_0 “piercing” the critical inclination. They are
 387 presented in Fig. 8 for model \mathcal{S} . Given that model \mathcal{J} is slightly perturbed, we just show the maps for $i_0 = 62^\circ 5$ and
 388 $i_0 = 65^\circ 2$ in Fig. 9. The maps have been computed on a 500×500 grid of initial conditions, forward in time, and over a
 389 time interval of 20 years. We have considered 4 values of the initial inclinations, namely $i_0 \in \{62^\circ 5, 63^\circ 4, 64^\circ 3, 65^\circ 2\}$.
 390 The initial phasing is set as $(\omega, \Omega) = (270^\circ, 0^\circ)$. If a given initial condition in the map fall within the highest region
 391 of the FLIs (yellow tone), then the orbit is hyperbolic and exhibit sensitive dependence upon the initial condition
 392 (*i.e.*, any orbit starting with an initial condition slightly different will have a long-term different future; the orbits
 393 will separate with time). We note that the i_0 -dependence of the \mathcal{J} model is quasi-absent. The model \mathcal{J} is very close
 394 to the integrable picture, in the sense that the splitting of the separatrix is weak. The latter is much more manifest
 395 for model \mathcal{S} , where we recall, the eccentricity and inclinations variables are no longer frozen. For increasing values
 396 of i_0 , we underline the growing asymmetry of the foldings near the saddle-like structure for the model \mathcal{S} . This
 397 particular structure transfers directly at the single orbit level: an orbit trapped within the hyperbolic layer is more
 398 likely to display U-turns intermittency phenomena towards the lower semi-major axis. This observation, based on
 399 the thin structures of the lobes detected with a variational dynamical indicator on our model, is also in agreement
 400 with the actual two-line elements datasets for objects M1-69 and M1-87.

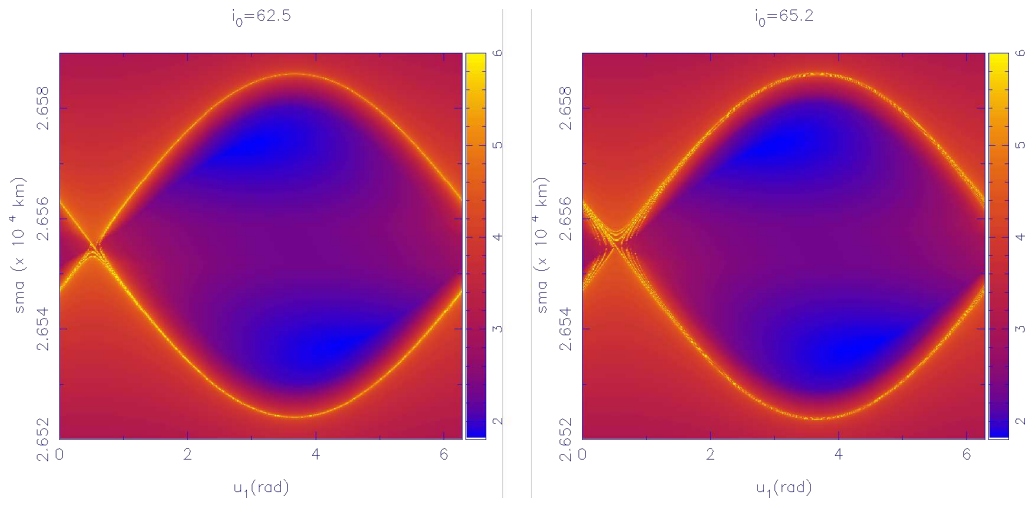


Fig. 9 Intersections of the forward in time FLIs with the plane (a, u_1) for model \mathcal{J} computed on a 500×500 grid of initial conditions for $i_0 \in \{62.5, 65.2\}$ deg.

Figures

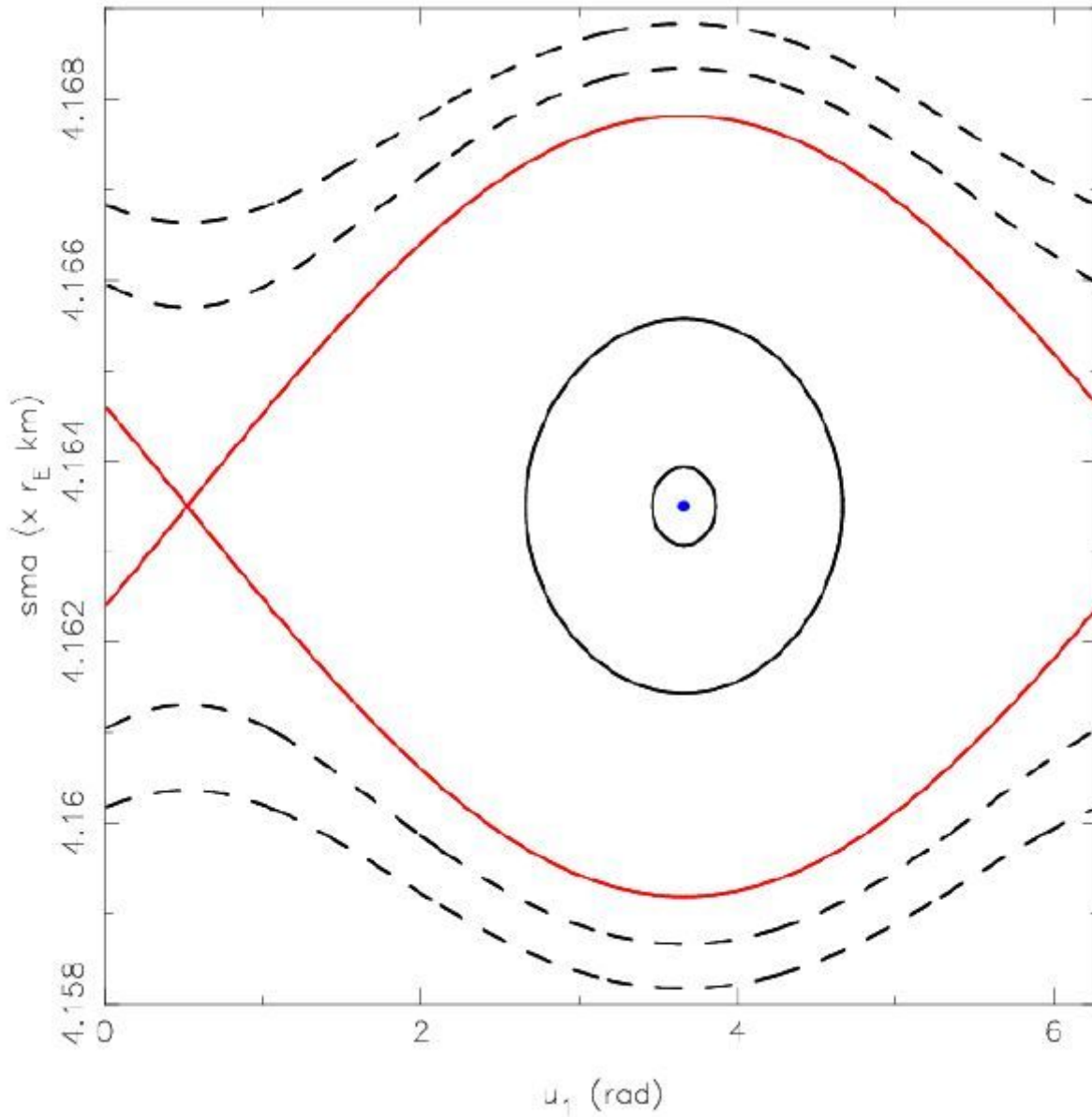


Figure 1

Phase space of the resonant integrable approximation. The width of the separatrix (red curve) allows excursion of the semi-major axis up to $2\Delta a = 54$ km within the libration domain. The oscillations near the elliptic fixed point (blue point) have a period of about 1:76 years.

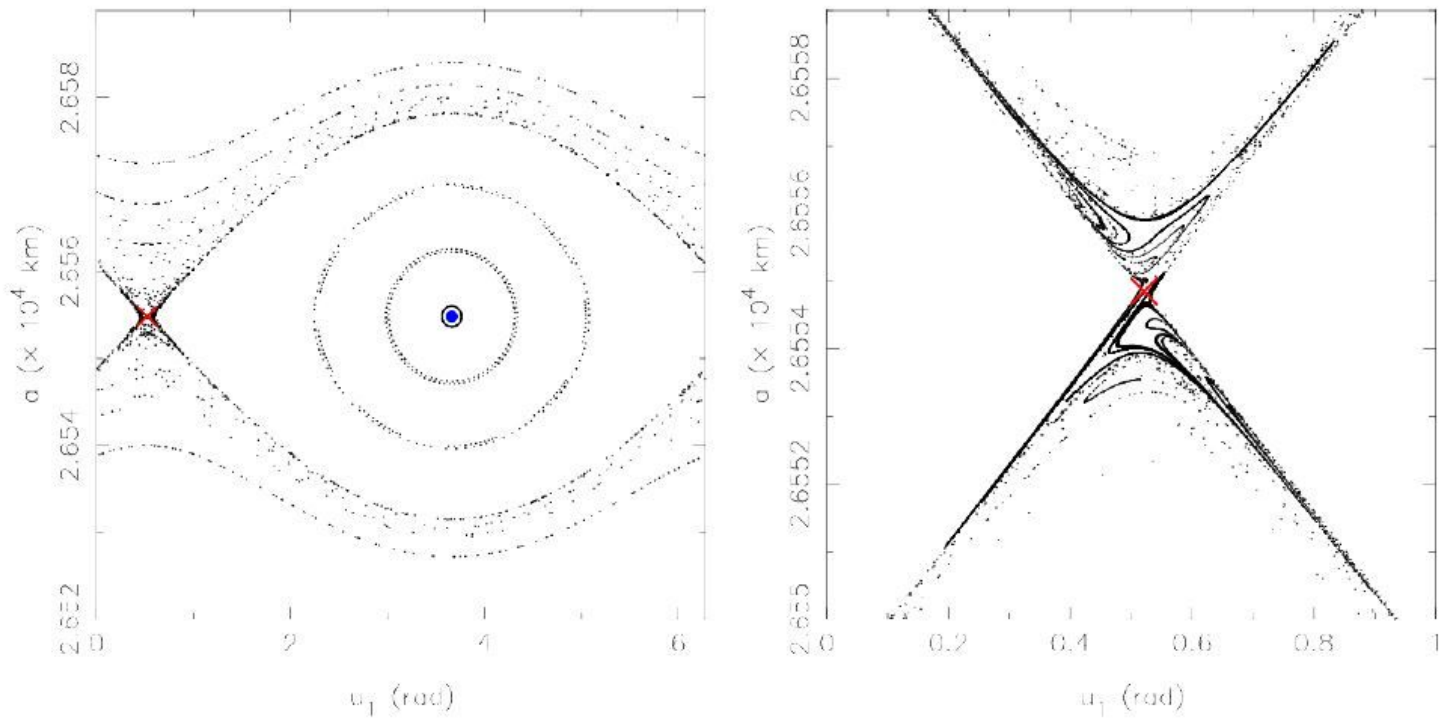


Figure 2

(Left) Poincaré section associated to (35) computed for $g(0) = 0$. The unstable fixed point is labeled with the red cross, the blue circle surrounds the stable periodic orbit. The phase space is similar to the integrable approximation but contains a thin chaotic layer (scattered erratic points) surrounding the unperturbed separatrix. Each considered initial condition has been iterated 100 times under P . (Right) Details of nice pieces of the stable manifold $W_s(x_u)$.

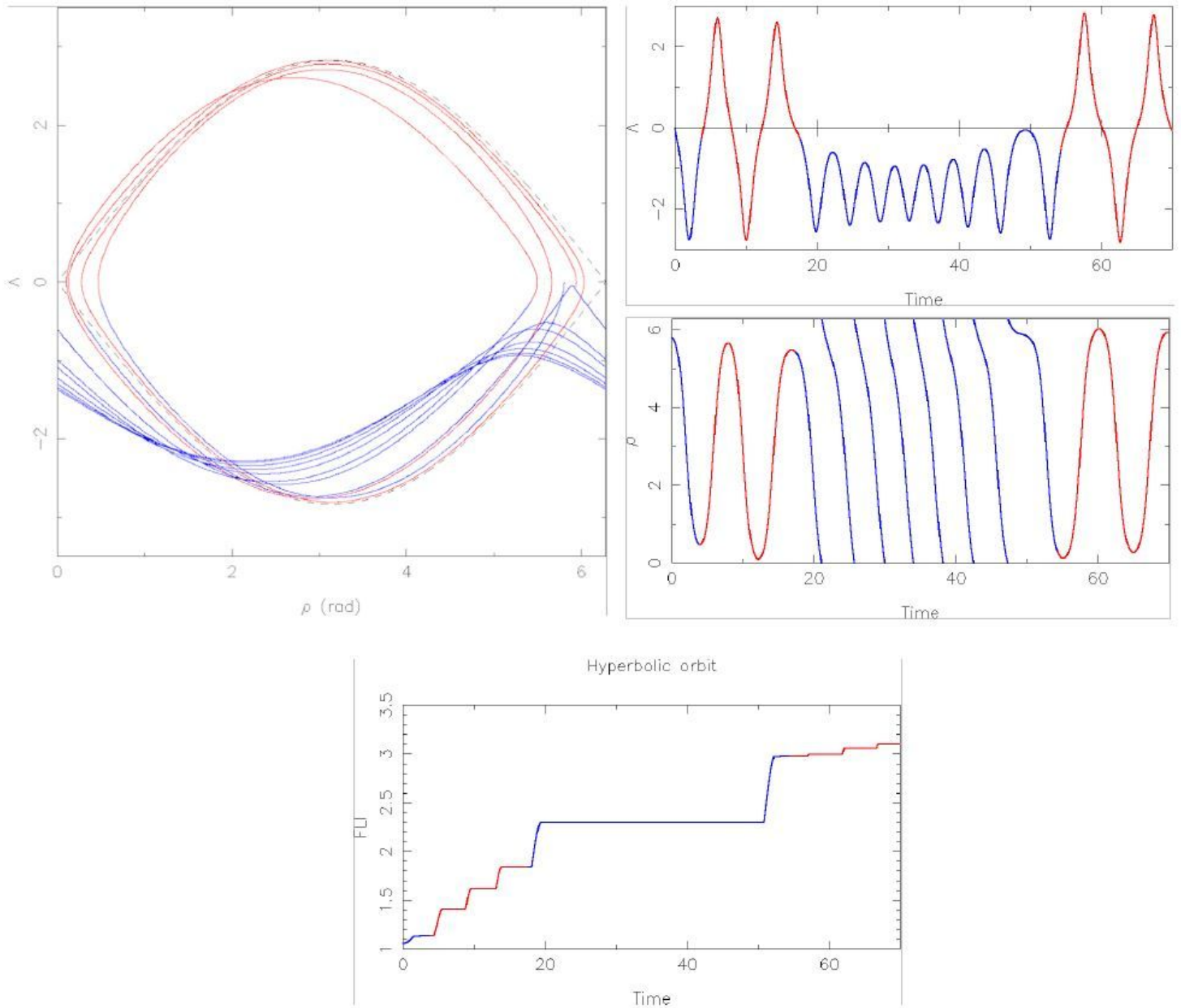


Figure 3

Composite plot illustrating the mechanisms of the intermittency phenomena. The dashed black line represents the separatrix of the integrable model T . Realisations of the stable and unstable manifolds, for $\epsilon \neq 0$; $\epsilon \ll 1$, are not shown for the sake of readability. One hyperbolic orbit trapped in the hyperbolic tangle is highlighted in the phase space, with a color code depending on the regime of the resonant angle. When the resonant angle circulates (blue color), $(p) \neq 0$, the action takes negative Δ 's. When the angle librates (red color), $(p) \sim 0$, the action variable performs the full homoclinic loop and exhibit larger variations. Alternation between circulation and librations with passage close to the saddle contribute to breaks the plateau structure of the FLI and produces jumps in the FLI.

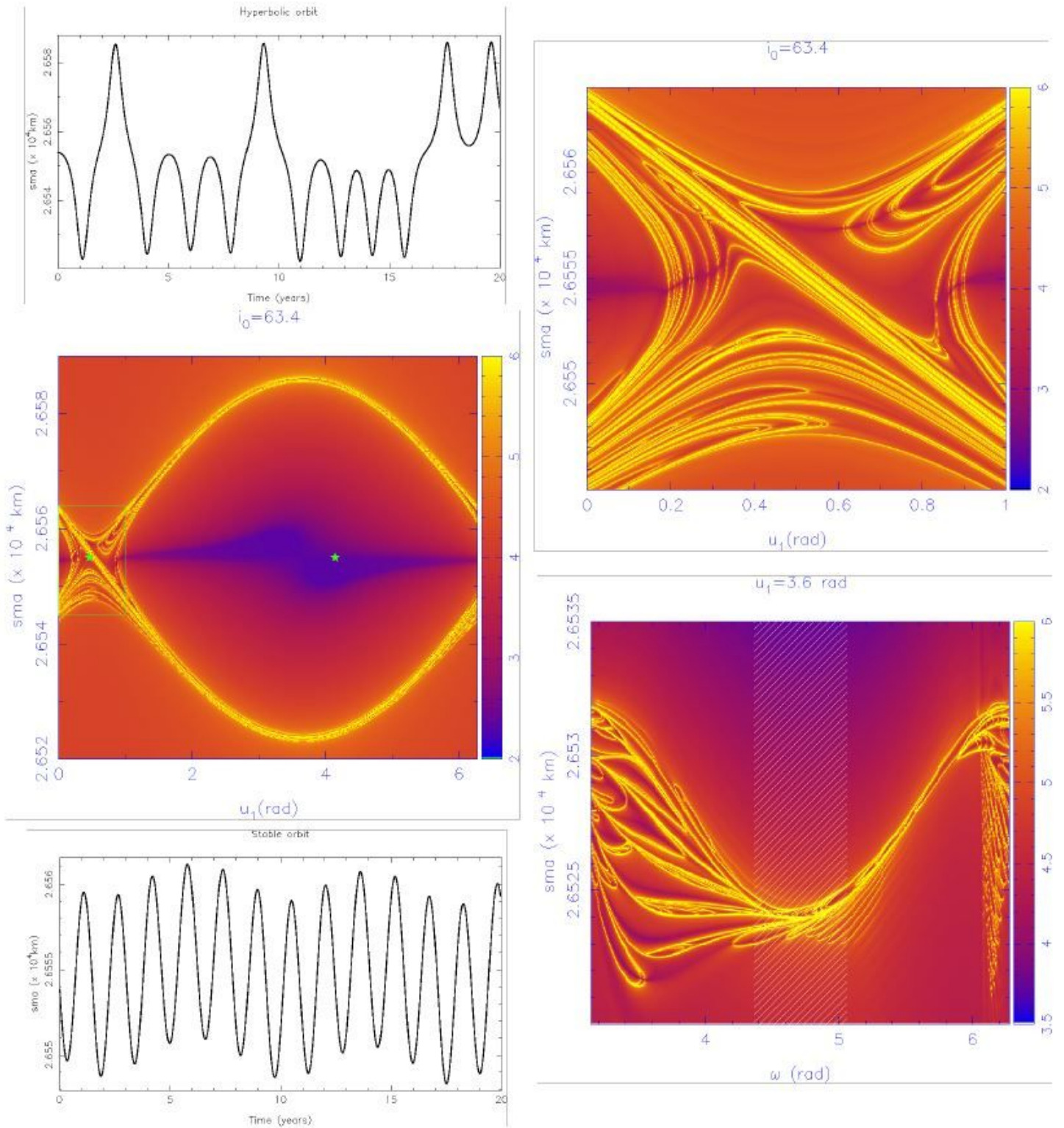


Figure 4

Composite plot highlighting the main features of Molniya semi-major axis dynamics. The global FLI map and a magnied portion near the saddle-like structure detail the hyperbolic structure. Initial conditions within the hyperbolic layer display intermittency phenomena, whilst stable orbits display regular oscillations. This is exemplified for two orbits whose initial conditions are labeled with the green stars. The width of the layer, for a xed u_1 but varying ω , might exhibit a complex geometry. For Molniya's

prototypical range of values of ω , materialised by the white shaded-line region around $\omega = 270^\circ$, the width is limited to a few kilometer in the semi-major axis only. See text for details.

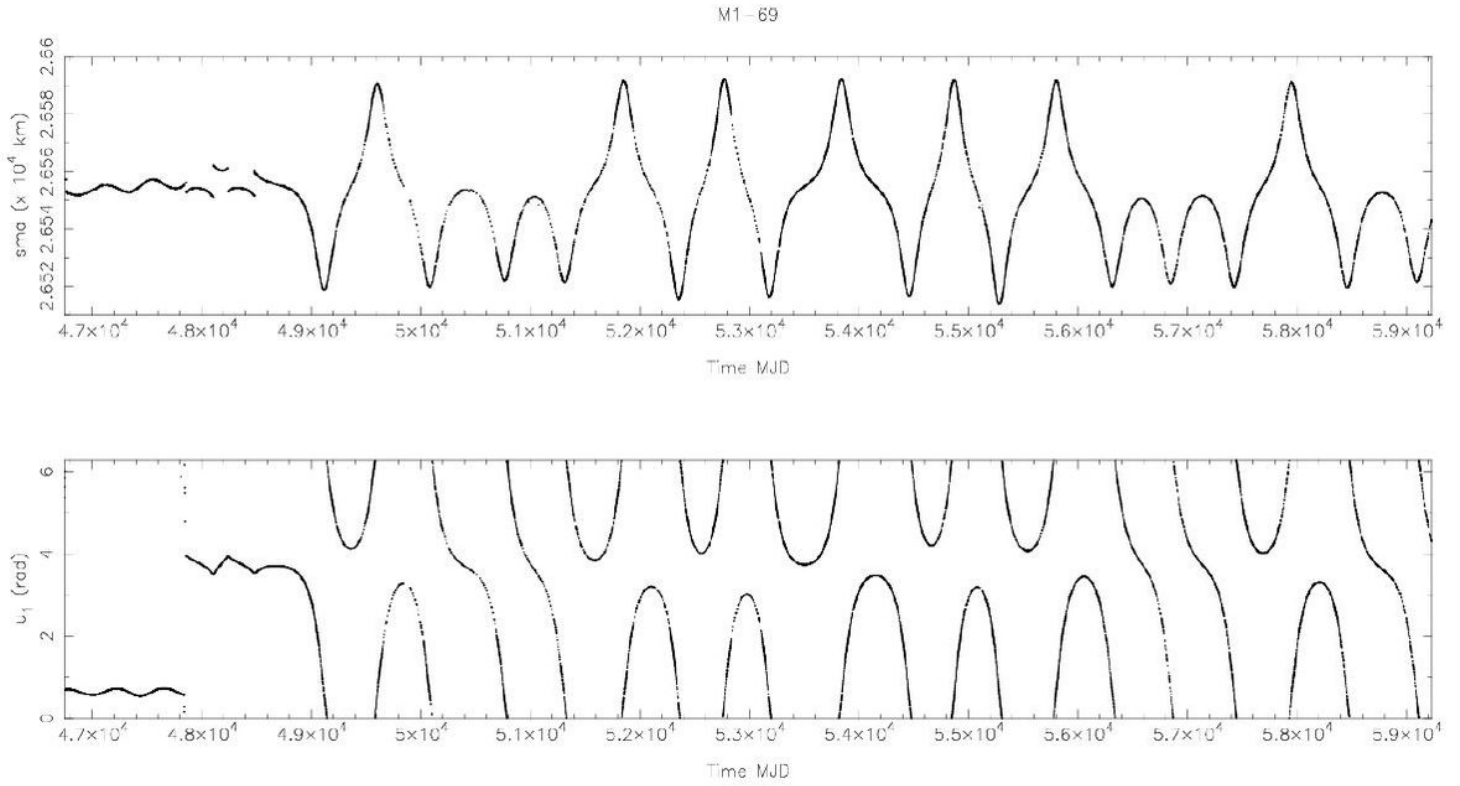


Figure 5

Time history of the semi-major axis and resonant angle u_1 extracted from the TLE data for the satellite M1-69.

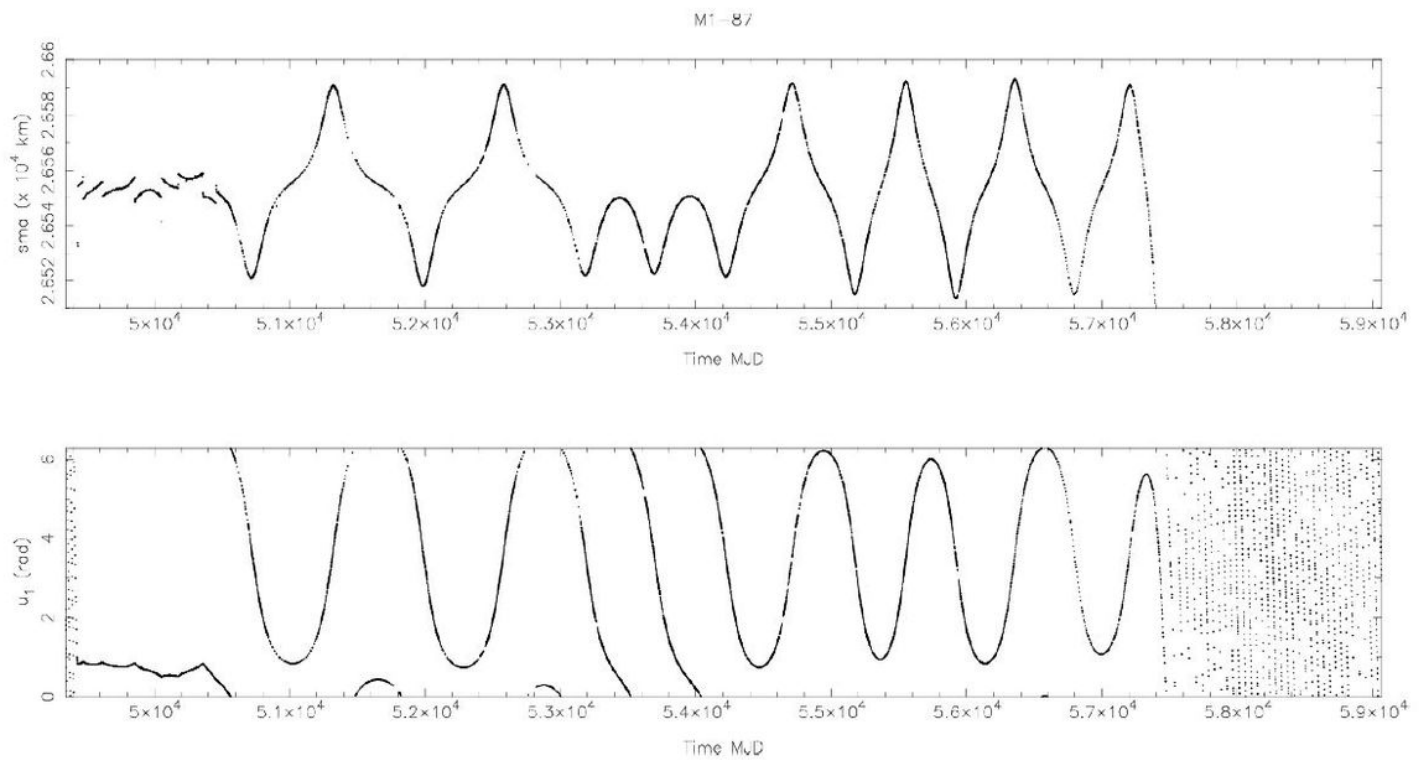


Figure 6

Time history of the semi-major axis and resonant angle u_1 extracted from the TLE data for the satellite M1-87

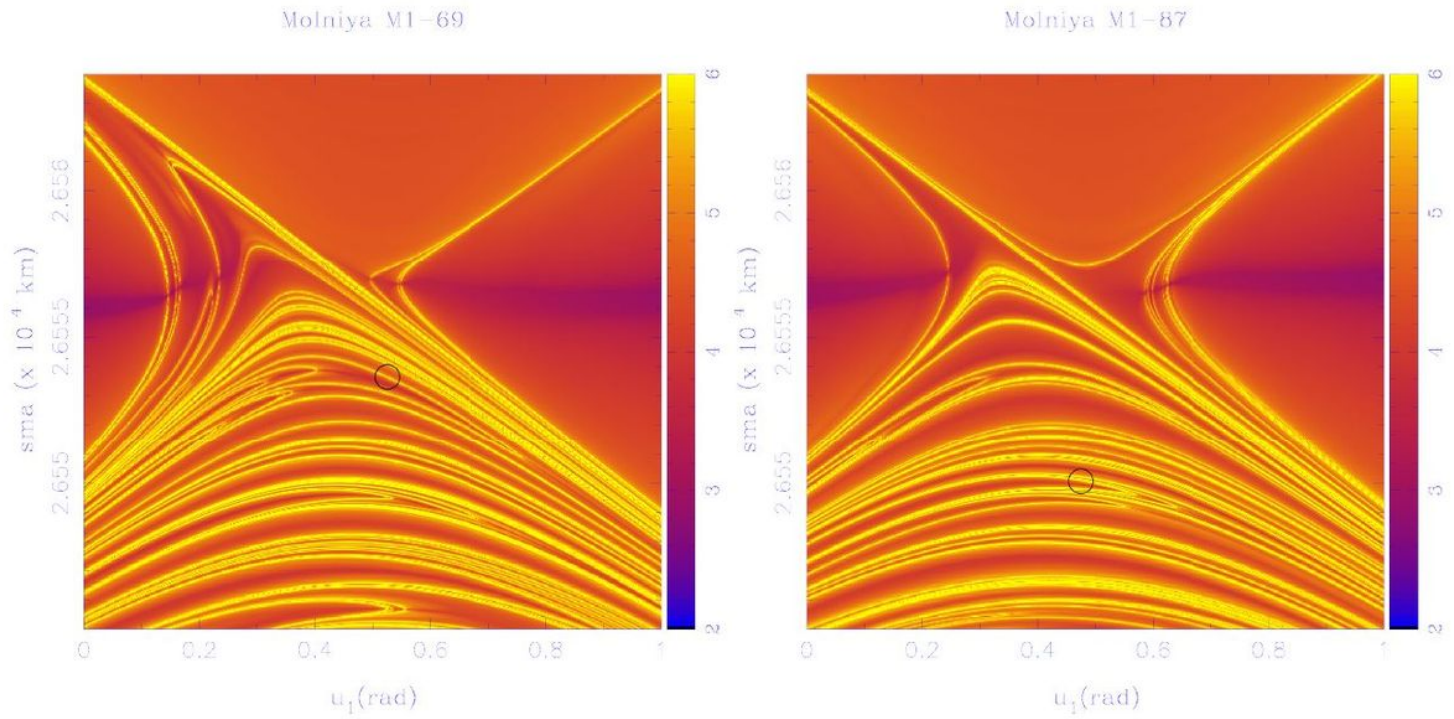


Figure 7

Dynamical maps for Molniya M1-69 and M1-87. The locations of M1-69 and M1-87 are marked through the black circle. Both satellites reside within the hyperbolic tangle.

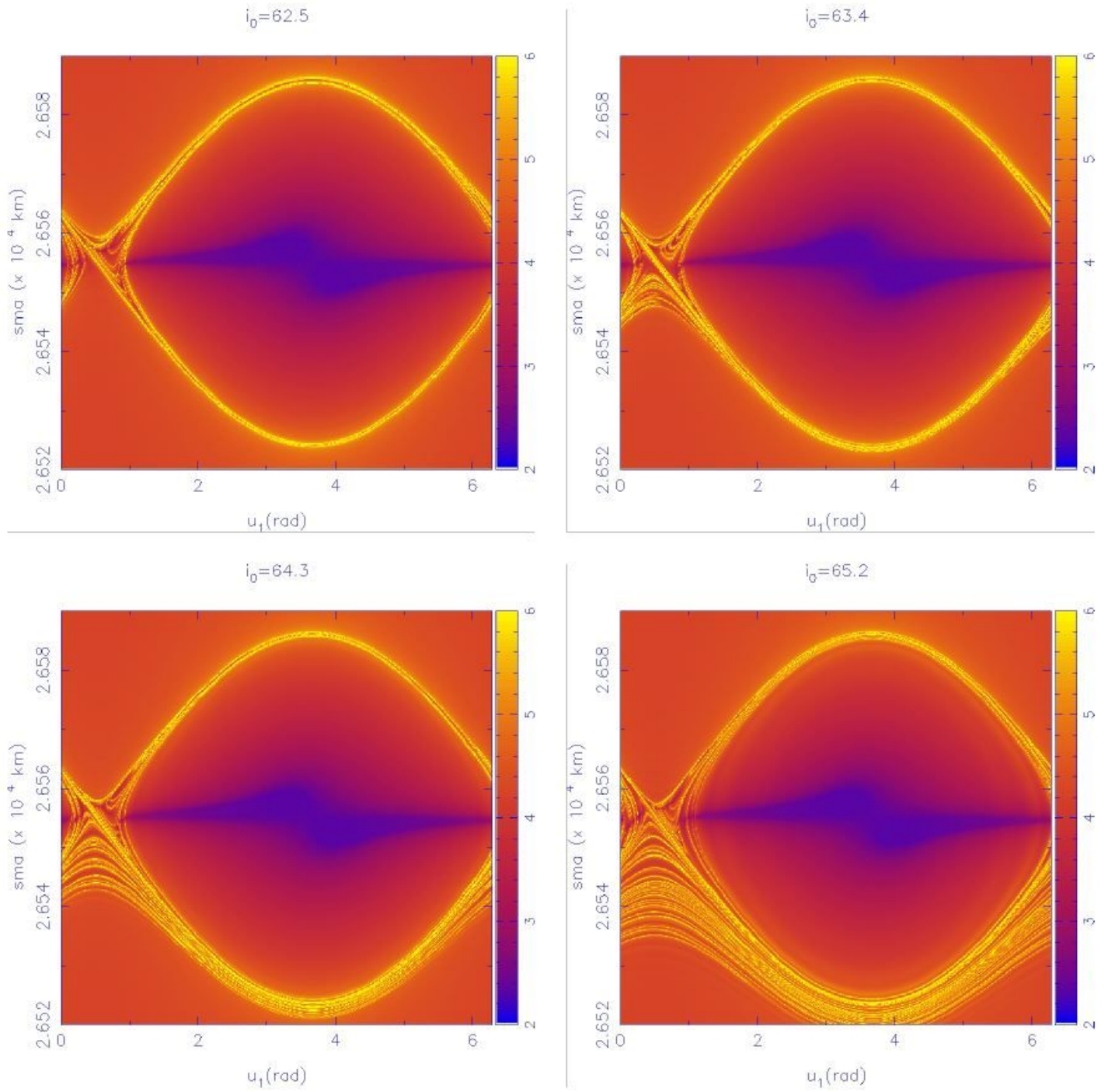


Figure 8

Intersections of the forward in time FLIs with the plane ($a; u_1$) for model S computed on a 500 x 500 grid of initial conditions for $i_0 \in \{62.5, 64.3, 64.3, 65.2\}$ deg.

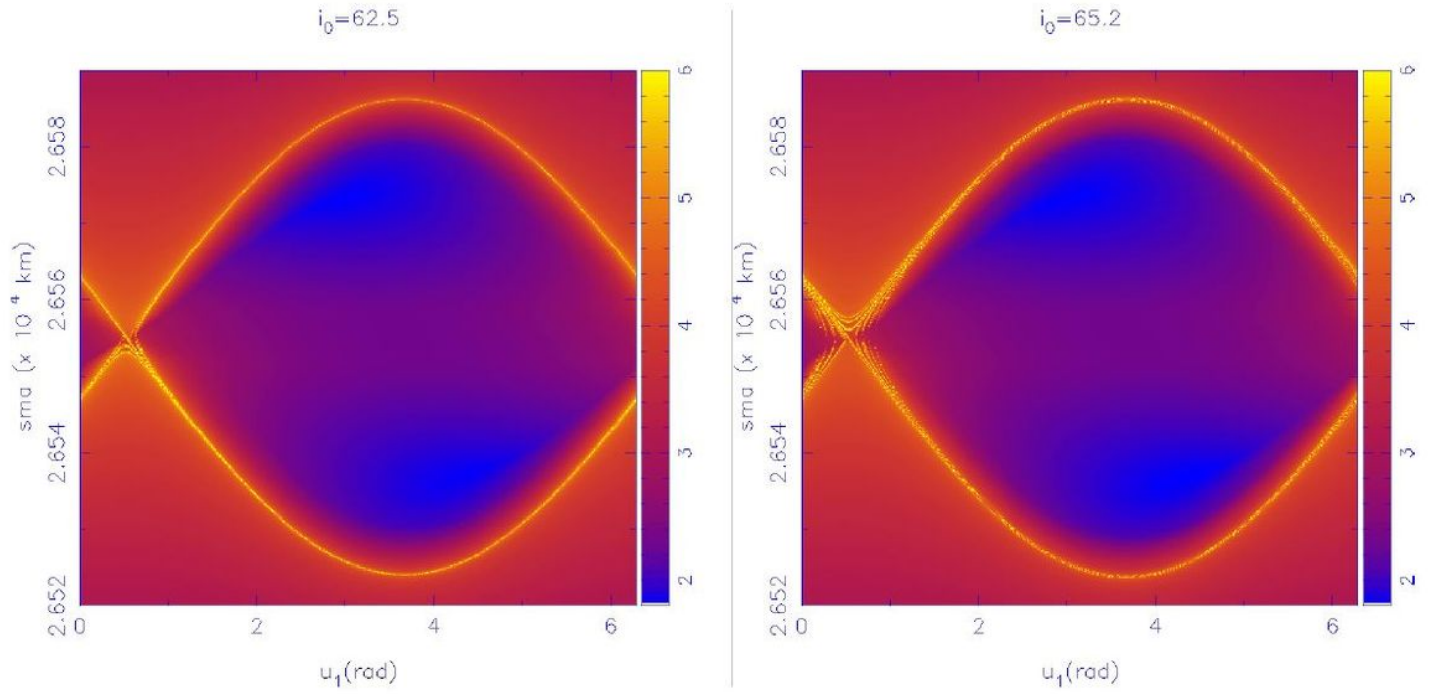


Figure 9

Intersections of the forward in time FLIs with the plane $(a; u_1)$ for model J computed on a 500x500 grid of initial conditions for $i_0 \in \{62.5, 65.2\}$ deg.